UNIVERSITÀ DEGLI STUDI DI MODENA E REGGIO EMILIA

Dottorato di ricerca in Ingegneria industriale e del territorio

Ciclo XXXV

Direct Numerical Simulation of wind-wave turbulence

Candidato: Federica Romoli

Relatore (Tutor): Enrico Stalio

Correlatore : Andrea Cimarelli

Contents

Abstract

After decades of research efforts, the wind-wave interaction mechanisms have been recognized as extremely elusive. The reason is the complex nature of the problem which combines complex coupling mechanisms between turbulent wind and water waves with the presence of multiple governing parameters such as the friction Reynolds number of the wind, the water depth and the wind fetch. As unequivocally shown here, the use of suitable flow settings allows to reduce the complex problem of wind-wave interaction to its essentials features mainly as a function of the sole friction Reynolds number of the wind. The resulting numerical solution allows to study the interactions between water and air layers with its own fluid properties and to unveil very interesting features such as an oblique wave pattern traveling upstream and a wave-induced Stokes sublayer. The latter is responsible for a drag reduction mechanism in the turbulent wind. Despite the simulated flow conditions are far from the intense events occurring at the ocean-atmosphere interface, the here unveiled basic flow phenomena may explain some experimental evidences in wind-wave problems. Among others, the wave-induced Stokes sublayer may shed light on the large scatter of the drag coefficient data in field measurements where swell waves of arbitrary directions are often present. Hence, the present results and the developed approach pave the way for the understanding and modeling of the surface fluxes at the ocean-atmosphere interface which are of overwhelming importance for climate science.

Chapter 1

Wind and ocean waves interactions

Momentum, heat, and mass exchanges between air and water are of primary importance for the characterization of geophysical flows and climate formation mechanisms. Field observation shows that, the presence of moving waves determines an interaction between the atmospheric boundary layer and the wave field developed in response to the wind forcing. These interactions influence the flux of momentum and and heat trough air–sea interface and alter the atmospheric boundary layer in the water proximity, modifying the classical features associated to a wall bounded flow. In analogy with flows over hills, the disturbances introduced by surface waves determine a surface deformation described by the wave length λ, the wave amplitude a and the wave steepness a/λ. However the impact of waves on the atmospheric boundary layer depend not only on their geometry but also on some peculiar aspects strictly related to the wave nature. First, the waves can be seen as undulations propagating through the sea surface therefore they are not stationary but evolve with a certain speed called phase speed c, that for a monocromatic wave is defined as the ratio between its wave frequency ω and its wave number k. Second, the waves grow and decay locally under the wind forcing, it means that their shape is not fixed but it is the result of a dynamic coupling between wind and waves. Third, a real sea surface is described by a broadbend spectrum: the wave state can not be studied by means of a monocromatic description because it is the sum of individual sinusoids, each moving at a different wave speed. This broadband nature of the wave state introduces some additional complexities such as the multiscale nature of the sea surface and the non linear interaction between different wave components.

Despite the extensive research activity on the topic, the present understanding of the physical mechanisms behind the wind wave interactions remains unclear.

1.1 Theoretical model of wave growth and evolution

1.1.1 Kelvin-Helmholtz theory

The first attempt to study the complex interactions, occuring in a two phase flow, was done by Kelvin and Helmholtz in 1880. They developed the irrotational theory of waves induced by the parallel movement of two fluids with different density (ρ_1, ρ_2) and velocities (u_1, u_2). Assuming the fluid to be two-dimensional, incompressible, irrotational, of unlimited depth, and considering small disturbances around the steady state of the boundary between the two fluids, a solution can be found for the wave growth rate. Considering the free surface wave height function as $\eta = ae^{i(\omega t - kx)}$,where ω is the wave angular frequency and k is the wave number,it is possible to find an expression for the phase speed of the wave defined as the ratio between ω and k:

$$\begin{aligned} c &= \bar{u} \pm \bar{c} \\ \bar{u} &= \frac{\rho_1 \bar{u}_1 + \rho_2 \bar{u}_2}{\rho_1 + \rho_2} \\ c^2 &= c_0^2 - \frac{\rho_1 \rho_2}{(\rho_1 + \rho_2)^2}(u_1 - u_2)^2 \\ c_0 &= \frac{g}{k}\frac{1 - \rho_1/\rho_2}{1 - \rho_1/\rho_2} \end{aligned} \tag{1.1}$$

where $\bar{u}$ and c are the averaged value of velocity between u_1 and U_2 phase speed, while c_0 is the phase velocity in correspondence of no current in both fluids ($U_1 = u_2 = 0$). The instability of a wave and so the wave growth can be observed from (1.1): when the phase velocity c becomes imaginary, the free surface height η progressively increase in amplitude leading to an unstable process. Considering the fluids of different densities to be air and water

$$\rho_a = 1kg/m^3 \quad \rho_w = 1000kg/m^3$$

and neglecting the contribution of the density ratio $\rho_a/\rho_w = 10^{-3}$, the instability condition will be:

$$u_1 - u_2 = u_a - u_w = u_c > c_0 \frac{1 + \rho_a/\rho_w}{\sqrt{\rho_a/\rho_a}} \approx 30\frac{g}{k} \tag{1.2}$$

The main problem of this theory, applied to the wind-wave interaction, arises from the value of the predicted critical velocity of u_c, that is the minimum wind relative velocity capable of generating instability, and so wave growth, does not match the reality: the smallest existing wave in the ocean spectrum usually have a phase velocity of 0.2 m/s. It means that the critical velocity would be $u_c = 30 \cdot 0.2 = 6m/s$.

So the waves will be stable until the relative velocity of the wind will reach $6m/s$. Nevertheless from direct observations, it well known that velocity of a wind just strong enough to rise waves is about $1,1m/s$.

1.1.2 Jeffreys sheltering theory

The first attempt to explain this discrepancy between theory and observations was given by Jeffreys in 1925 with his sheltering theory (Jeffreys, 1925). He abandoned the irrotational hypothesis on air and realized that the interaction between wind and wave cause the inability of the wind to follow the deformed water free surface. The resulting airflow separation on the leeside of the wave leads to a pressure drop and hence to a recirculation zone (the "sheltered zone") in the proximity of the wave trough. According to Jeffreys the fluctuating pressure distribution is the main responsible for the wave growth and the force applied to the free surface can be evaluated by:

$$F = s\rho_a u_a^2 \frac{d\eta}{dx} \tag{1.3}$$

where s is the sheltering constant, u_a the wind velocity over the crests and η is the wave elevation. The formula (1.3) is called "the sheltering hypothesis" and comes from the analogy of this problem with the one of the thrust produced by a current over an inclined lamina in the direction of the flow. There were two problems in this theory: the former was the assumption of no tangential stresses, thus no air friction acting along the free surface; the latter was that the observed value of the constant s, made by solid wave models, was smaller than what predicted by the sheltering model and the resulting force caused by the wind in the sheltered zone, was not enough to let waves grow.

1.1.3 Philips and Miles theories

Phillips(1957) and Miles (1957) proposed two mechanisms which aim at explaining the initial and the later stage of wave growth, respectively (Phillips, 1957; Miles, 1957). The mechanism proposed by Philips considers the crucial role of turbulence in the wave generation. Considering an infinite sheet of deep inviscid water, initially at rest, he found that waves develop most rapidly by means of a resonance mechanism which occurs when a component of the fluctuating air pressure field moves with the same speed of the water free surface with the same wave number. This growth mechanism continues until waves grow so high that non-linear effects, established between wind and wave, become important. The Philips' resonance mechanism predict a linear wave growth with time:

$$\overline{\eta^2} \sim \frac{\overline{p'^2} t}{2\sqrt{2\rho_w^2 U_c g}} \tag{1.4}$$

where $\overline{\eta^2}$ is the mean square surface displacement, $\overline{p'^2}$ is the mean square turbulent pressure on the water surface, t the elapsed time, U_c the convective speed of the surface pressure fluctuation and ρ_w the water density. In parallel with the Phillips theory, was developed another important theory by Miles. The hypothesis behind this theory regard both air and water phase. The air is assumed to be inviscid, incompressible and, in the absence of the wave motion, to have a prescribed mean shear flow $U(y)$, where y is the vertical coordinate. The water is considered inviscid, incompressible and with a small surface slope (ak) to permit the equations linearization. Although the turbulent nature of the wind seems to be decisive in the the dynamics of the system, Miles constructed a model which neglects the interaction between turbulence and wave-induced perturbations. Due to this hypothesis the wind-wave interaction is described by the Orr-Sommerfeld equation that, for inviscid fluids, becomes the Rayleigh's equation. By following the stability analysis, he found that for air flowing a wavy surface, there is a critical height y_c , where the unperturbed wind speed, $U(y)$, equals the real part of wave phase speed c.The concept of the critical layer is crucial in the Miles theory. As a matter of fact it represents the height at which the energy transfer from the wind to the waves is concentrated. The rate of energy transfer can be expressed as:

$$r = -\pi(U''|_{y=y_c}/kU'|_{y=y_c})/(\overline{W^2}) \tag{1.5}$$

From the above expression it is clear that r is proportional to the velocity profile curvature at the critical layer, i.e. to $U''(y)$ at y_c. From a physical point of view the transfer of energy can be explained as follow: the upward motion of the air flow over the waves induces a sinusoidal pressure variation which in turns leads to a closed loop structures (cat's eye) of periodically varying strength forming at the critical height. Then the vortex force on the wave leads to a transfer of energy from the wind to the waves. Two are the criticisms of Miles' theory: the former is that the energy transfer is concentrated in the critical layer, which has an infinitesimal thickness and the latter is related to the location of the critical height. As a matter of fact the critical layer is very close to the surface of the wave, which means that the critical layer height is well within the inner surface layer. Hence, the overall energy transfer from wind to waves is very small.

1.1.4 The Non-Separated Sheltering (NSS) mechanism

Now the question is: Does the critical layer plays a significant role in turbulent flows over a wave? For slowly or rapidly moving waves, Belcher & Hunt (1993) discussed the importance of nonseparated sheltering. They divided the airflow into an inner region and an outer regions. Close to the interface is an inner region

where the wave-induced turbulent shear stress significantly affects the wave-induced mean flow, which leads to a sheltering effect, whereby streamlines are displaced asymmetrically about the wave crest. In an outer region, turbulence is advected over a wavelength too rapidly for it to transport significant momentum and so the wave-induced flow there is inviscid to a good approximation.

In the inner region the turbulent eddies have sufficient time to interact before they are advected by the mean flow and they reach a local equilibrium state. In this region, the effects of the shear stress displace the streamlines asymmetrically causing the turbulent boundary layer thickening and an asymmetric pressure distribution that, again, leads to wave growth.

In the outer region, the turbulent eddies are advected rapidly before they interact with other. It means that turbulent perturbations are small and linear approximation can be applied, better satisfying the assumption of the critical-layer mechanism. In the nonseparated sheltering mechanism, momentum transfer from the air flow to the waves is determined by the flow asymmetry, caused by the perturbation of the shear stress in the inner region. In the critical-layer mechanism, the perturbations near the wave surface are determined by the perturbations of the airflow at the critical height, caused by the wave-induced velocity. It is important to say that nonseparated sheltering mechanism does not exclude or substitute the Miles' one. In fact, they both work together, but the effectiveness of each one depends on the wave speed c (or wave age). Therefore, we can identify three types of waves: slow, intermediate and fast. For slow waves the critical layer is very close to the surface and his effect towards the rest of the flow is negligible; here prevails the non-separated sheltering. The more the waves grow the more the critical layer moves upwards, until its influence on the mean flux is negligible; stated this, we can say that even in the case of fast waves the prevailing mechanism is the non-separated sheltering one. Finally, for intermediate wave speeds, the critical height is roughly situated in the transition zone between the inner and outer region of the flux and its role cannot be neglected. In this case the relation among the two mechanisms is complex and needs more investigation.

Chapter 2

DNS of a two phase pressure driven channel

The complexity of the problem makes the wind-wave interactions difficult to be numerically represented. The aim of the present chapter is to overcome some of the previous mentioned issues by considering a numerical simulations of a turbulent wind blowing over a water free surface. In the present simulation the two-phases are dynamically evolved based on first principles and the multiplicity of the governing parameters is reduced to the sole Reynolds number of the wind, thus addressing the problem at equilibrium, i.e. for infinite wind fetch lengths. The chapter is organized as follows. In section §1, the numerical method and the flow settings are described. In section §3, the water wave pattern is characterized while, in sections §4 and §5, the turbulent wind boundary layer is analysed. The influence of the wind-wave mechanisms on the field of stresses in the wind boundary layer is addressed in section §6. Finally, the paper is closed by final remarks in section

2.1 Equations and numerical methods

The flow evolution is governed by the continuity and momentum equations. The evolution of the flow is governed by the continuity and momentum equations. This set of equations is solved here in a *one-fluid formulation* where the same set of equations is applied for two immiscible fluids with different density ρ and viscosity $\nu = \mu/\rho$,

$$\begin{cases} \dfrac{\partial u_i}{\partial x_i} = 0 \\ \dfrac{\partial \rho u_i}{\partial t} + \dfrac{\partial \rho u_i u_j}{\partial x_j} = -\dfrac{\partial p}{\partial x_i} + \dfrac{\partial \tau_{ij}}{\partial x_j} + f_{\sigma_i} + \rho g_i \end{cases} \tag{2.1}$$

where u_i is the velocity field, p is the pressure field, $\tau_{ij} = 2\mu S_{ij}$ is the viscous stress tensor with S_{ij} the strain rate tensor, f_i is the surface tension force and g_i the gravity acceleration. In the following the index $i = 1, 2, 3$ corresponds to the streamwise, vertical and spanwise directions and velocity components, (x, y, z) and (u, v, w) respectively. The evolution equations of the flow have been numerically solved by means of a finite volume discretization method using a structured Cartesian grid of hexahedral cells. The numerical technique is based on central spatial interpolation operators of the second order whereas time integration is performed with a first-order implicit Euler scheme. The pressure–velocity coupling is performed with the pressure-implicit split-operator algorithm (Issa, 1986). In order to identify the interface between the two fluids, a transport equation for the volume fraction function α ($\alpha = 1$ in the water phase and $\alpha = 0$ in the air phase) is coupled with the momentum equation (Hirt & Nichols, 1981),

$$\frac{\partial \alpha}{\partial t} + \frac{\partial u_j \alpha}{\partial x_j} + \frac{\partial}{\partial x_j}\left[\alpha\big(1-\alpha\big)\, u_{r_j}\right] = 0 \tag{2.2}$$

The numerical challenge of keeping the interface sharp is addressed by limiting the phase fluxes based on the "Multidimensional universal limiter with explicit solution" (MULES) limiter and by using a numerical interface compression method. The latter is expressed by the last term of (2.2) from which it is easy to recognize that is active only in the interface region due to the term $\alpha(1-\alpha)$. In the volume fraction equation (2.2), $\boldsymbol{u_r}$ is a compression velocity evaluated as

$$\boldsymbol{u_r} = c_\alpha \, |\boldsymbol{u}| \, \boldsymbol{n} \tag{2.3}$$

where

$$\boldsymbol{n} = \frac{\nabla \alpha}{|\nabla \alpha|} \tag{2.4}$$

is the unit normal to the interface vector and c_α is a compression coefficient that determines the strength of the compression, i.e. $c_\alpha = 0$ no compression, $c_\alpha = 1$ conservative compression and $c_\alpha > 1$ high compression (Okagaki *et al.*, 2021).

The volume fraction α from (2.2) is then used to compute the physical properties of the two fluids,

$$\rho = \rho_w \alpha + \big(1-\alpha\big)\rho_a \tag{2.5}$$

$$\mu = \mu_w \alpha + \big(1-\alpha\big)\mu_a \tag{2.6}$$

where the pedices w and a are used to denote quantities computed for water and air, respectively. The volume fraction α is also used to compute the local curvature of the interface, $\kappa = -\partial n_i / \partial x_i$. This observable is then used to model the surface tension (Brackbill *et al.*, 1992) as

$$f_i = \sigma \kappa \, n_i \tag{2.7}$$

where σ is the surface tension coefficient. In the present work, we consider air and water as working fluids for which standard values of viscosity and density are employed, $\nu_a = 1.48 \cdot 10^{-5}$, $\nu_w = 1 \cdot 10^{-6}$, $\rho_a = 1$, $\rho_w = 1 \cdot 10^3$ and $\sigma = 0.07 N/m$. It is important to highlight that the here reported solution of the wind-wave problem based on first principle equations with the actual properties of air and water represents an unicuum in the panorama of numerical simulations. Indeed, air and water introduce a sharp jump of the fluid properties at the interface thus representing a challenge for numerical techniques as demonstrated by a series of works where the jump between the two fluid properties have been reduced to obtain numerical stability, see e.g. Liu *et al.* (2022); Scapin *et al.* (2022), or where the evolution of the two fluids is separately integrated in time and their interaction is taken into account with suitable boundary conditions, see e.g. Yang & Shen (2010, 2011). Here, we success in obtaining a stable solution of the wind-wave problem based on first principle equations with the actual properties of air and water. To achieve this result a relevant role has been played by the value of the compression factor, $c_\alpha = 0.5$, in combination with the use of high resolution levels at the interface as better shown in the following section.

2.2 Flow settings

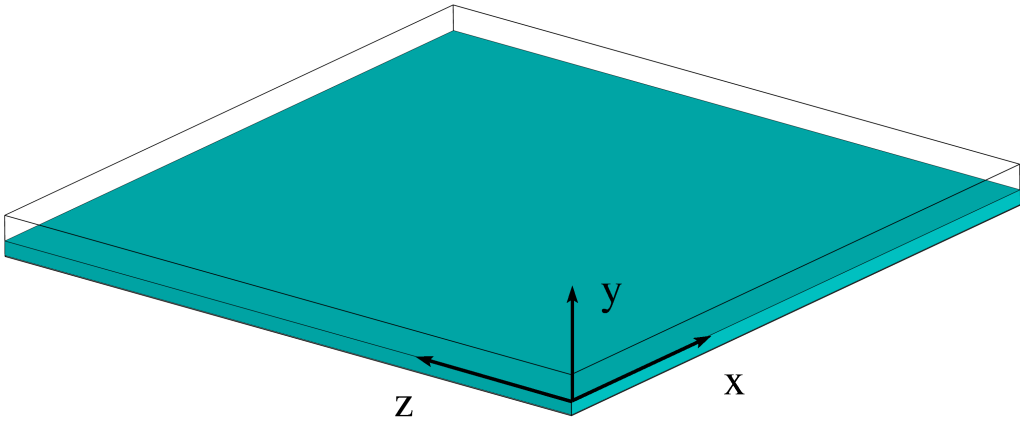

Figure 2.1: Numerical domain setup and Cartesian frame of reference.

The flow case considered is an open channel composed by a water layer on the bottom of an air layer on the top, see figure 2.1. Periodic boundary conditions are applied in the streamwise and spanwise directions for both velocity and volume fraction fields. No slip and free slip boundary conditions are imposed in the water bed

and top boundary, respectively. Finally, a zero gradient condition is imposed in the vertical direction for the volume fraction. The flow is driven by imposing a constant pressure gradient in the streamwise direction, dP_b/dx. This pressure gradient determines the friction Reynolds number of both the wind and water boundary layers, see §3. Accordingly, their ratio is completely determined solely by the heights of the air and water layers and by the properties of the two fluids,

$$\frac{Re_{\tau_a}}{Re_{\tau_w}} = \frac{\mu_w}{\mu_a}\sqrt{\frac{\rho_a}{\rho_w}}\sqrt{\frac{h_a^3}{(h_a+h_w)\,h_w^2}} \tag{2.8}$$

see again §3. Here, $Re_{\tau_a} = u_{\tau_a} h_a/\nu_a$ and $Re_{\tau_w} = u_{\tau_w} h_w/\nu_w$ are the friction Reynolds numbers of the air and water boundary layers, respectively, with $u_{\tau_a} = \sqrt{\langle \tau_{12} \rangle / \rho_a}$ and $u_{\tau_w} = \sqrt{\langle \tau_{12} \rangle / \rho_w}$ the air and water friction velocities evaluated at the interface between the two fluids (see section 5 for its exact definition) and at the water bed, respectively. In the present flow settings we have $Re_{\tau_a} = 317$ and a ratio $Re_{\tau_a}/Re_{\tau_w} \approx 3$. In conclusion, the choice of forcing coupled with the use of periodic boundary conditions allows us to obtain in a very simple and computationally efficient way, a fully developed turbulent boundary layer on top of an almost quiescent and laminar water layer.

The extent of the numerical domain is $(L_x, L_y = h_a + h_w, L_z) = (25.6h_a, 1.6h_a, 25.6h_a)$, where h_a and h_w are the heights of the air and water portions of the domain, respectively. The domain is discretized by means of a number of volumes $(N_x, N_y, N_z) = (820, 277, 1232)$ that are homogeneously distributed in the horizontal directions whereas stretching laws have been applied in the vertical direction in order to have larger resolution values in the highly inhomogeneous regions, i.e. at the wind-wave interface region. The resulting resolution in friction units is $(\Delta x^+, \Delta y^+_{min}, \Delta z^+) = (9.9, 0.1, 6.6)$, where Δy^+_{min} is achieved at the wind-wave interface. Throughout the paper, variables in friction units will be denoted with the superscript $+$, implying normalization of lengths with ν_a/u_{τ_a} and velocities with u_{τ_a} where the friction velocity u_{τ_a} is computed in a suitable plane at the wind-water interface as shown in section §5. On the other hand, when not specifically stated, variables will be reported dimensionless by using h_a for lengths and U_e for velocities where U_e is the average velocity at the top boundary. Finally, the time step is kept variable throughout the simulation to obtain a condition $CFL < 1$ in each point of the domain. The resulting time step, on average, is $\Delta t^+ = 1.1 \times 10^{-4}$.

In the present flow settings, the computational demand for well-converged statistics is mitigated by the statistical stationarity of the flow field and by the statistical homogeneity in the streamwise and spanwise directions. Hence, the average operator, hereafter denoted as $\langle \cdot \rangle$, combines a spatial average in the horizontal directions and a temporal average over 34 samples collected every $\Delta T^+ = 95$ after reaching a fully developed statistical state. In order to reduce the time needed by the flow

to reach a fully developed state, the simulation has been initialized by using the velocity fields from a precursory simulation of a single-phase turbulent open channel. This initialization is applied only for the air portion of the domain while the water one is initialized with a null value for velocity. In what follows, the customary Reynolds decomposition of the flow in a mean and fluctuating field will be adopted, i.e. $u_i = U_i + u_i'$ where capitol letters and the superscript $'$ will denote average and fluctuating quantities, respectively.

In closing this section, let us notice that the flow configuration here considered allows us to study the autonomous development of the wind-wave turbulence problem with air and water as working fluids. Indeed, the only parameters governing the flow are the imposed constant pressure gradient dP_b/dx and the ratio between the air boundary layer thickness and the water depth h_a/h_w being the thermodynamic properties of the fluids prescribed by the selection of air and water in standard conditions as working fluids. Hence, contrary to several previous attempts where the wave field is prescribed a priori or approximated with specific wave equations, see e.g. Sullivan *et al.* (2000), Kihara *et al.* (2007), Yang & Shen (2009), Yang & Shen (2010), Druzhinin *et al.* (2012), Yang *et al.* (2013), Sullivan *et al.* (2014) and Cao & Shen (2021), the present configuration allows us to prescribe only the general flow conditions, dP_b/dx and h_a/h_w, and to address the natural evolution based on first principles of wind and waves with air and water as working fluids in a fully coupled framework. To our knowledge, this is the first attempt of this kind.

Chapter 3

Flow symmetries and mean equations

The configuration of the two-phase open channel considered in the present work exhibits certain statistical symmetries that can be exploited to specialize the mean flow equations. Indeed, by considering fully developed conditions we have that the average flow solution is invariant under translations in time and in the streamwise and spanwise spatial directions. Furthermore, we have that the average surface tension and also the gravity term have a non-zero contribution only in the vertical direction, i.e. $\langle f_{\sigma_1} \rangle = \langle f_{\sigma_3} \rangle = 0$ and $\rho g_1 = \rho g_3 = 0$. All these symmetries allow us to reduce the problem of wind-wave interactions to its essential features. The mean flow equations read

$$\begin{cases} \dfrac{\partial \langle u_i \rangle}{\partial x_i} = 0 \\ \dfrac{\partial \langle \rho \rangle \widetilde{u}_i}{\partial t} + \dfrac{\partial \langle \rho \rangle \widetilde{u}_i \, \widetilde{u}_j}{\partial x_j} = -\dfrac{\partial \langle p \rangle}{\partial x_i} + \dfrac{\partial \langle \tau_{ij} \rangle}{\partial x_j} - \dfrac{\partial \langle \rho u_i'' u_j'' \rangle}{\partial x_j} + \langle f_{\sigma_i} \rangle + \langle \rho g_i \rangle \end{cases} \tag{3.1}$$

where the Favre average $\widetilde{\boldsymbol{u}} = \langle \rho \boldsymbol{u} \rangle / \langle \rho \rangle$ and the Favre fluctuation $\boldsymbol{u}'' = \boldsymbol{u} - \widetilde{\boldsymbol{u}}$ have been introduced to take into account the density variations at the air-water interface region. By taking into account the above mentioned statistical symmetries of the flow, the mean flow equations become

$$\begin{cases} \dfrac{dV}{dy} = 0 \\ \dfrac{d\langle \rho \rangle \widetilde{u} \, \widetilde{v}}{dy} = -\dfrac{\partial P}{\partial x} + \dfrac{d\langle \tau_{12} \rangle}{dy} - \dfrac{d\langle \rho u'' v'' \rangle}{dy} \\ \dfrac{d\langle \rho \rangle \widetilde{v} \, \widetilde{v}}{dy} = -\dfrac{\partial P}{\partial y} + \dfrac{d\langle \tau_{22} \rangle}{dy} - \dfrac{d\langle \rho v'' v'' \rangle}{dy} + \langle f_{\sigma_2} \rangle + \langle \rho g_2 \rangle \\ \dfrac{d\langle \rho \rangle \widetilde{w} \, \widetilde{v}}{dy} = \dfrac{d\langle \tau_{32} \rangle}{dy} - \dfrac{d\langle \rho w'' v'' \rangle}{dy} \end{cases} \tag{3.2}$$

where capitol letters are introduced to denote average quantities. From the continuity equation we have the trivial result $V = 0$. The above equations (3.2) allow us to define the behaviour of the average normal and shear stresses. In the following, to better express the corresponding equations we consider a shift of the origin of the wall normal coordinate to the water bed, $\hat{y} = y + h_w$.

By considering the integral of the momentum equation in the vertical direction, we can write an equation for the average pressure field,

$$P = P_b - \langle\rho\rangle\widetilde{v}\,\widetilde{v} + \langle\tau_{22}\rangle - \langle\rho\, v''v''\rangle + \int_0^{\hat{y}} \langle f_{\sigma_2}\rangle\, dy + g_2 \int_0^{\hat{y}} \langle\rho\rangle\, dy \tag{3.3}$$

where P_b is the average pressure field at the water bed $\hat{y} = 0$. An important consequence of this equation is that the mean streamwise pressure gradient is uniform across the two fluids,

$$\frac{\partial P}{\partial x} = \frac{dP_b}{dx} \tag{3.4}$$

In the vertical stress balance (3.3), it is important to highlight that some terms have a non-null contribution only at the interface region between the two fluids. These terms are $\langle\rho\rangle\widetilde{v}\,\widetilde{v}$, $\langle\tau_{22}\rangle$ and $\langle f_{\sigma_2}\rangle$. Furthermore, outside the interface region we also have that $\langle\rho\, v''v''\rangle$ reduces to the classical Reynolds stress, i.e. $\langle\rho\, v''v''\rangle = \langle\rho\, v'v'\rangle$. By taking into account these considerations, we can write that

$$P = P_b - \rho_w\langle v'v'\rangle + \rho_w g_2\, \hat{y} \qquad \text{for } \hat{y} < h_{int}^{<} \tag{3.5}$$

and

$$\begin{aligned} P =& P_b - \rho_a\langle v'v'\rangle + \int_{h_{int}^{<}}^{h_{int}^{>}} \langle f_{\sigma_2}\rangle\, dy + \rho_w g_2 h_{int}^{<} + \\ & \rho_a g_2\big(\hat{y} - h_{int}^{>}\big) + g_2 \int_{h_{int}^{<}}^{h_{int}^{>}} \langle\rho\rangle\, dy \qquad \text{for } \hat{y} > h_{int}^{>} \end{aligned} \tag{3.6}$$

where $h_{int}^{<} < \hat{y} < h_{int}^{>}$ is the region of the flow where the fluid properties change. The thickness of this layer, $\delta_{int} = h_{int}^{>} - h_{int}^{<}$, depends on the height of the wave motion δ_w and on the thickness of the interface between the two fluids. Being the latter generally small, a good approximation is $\delta_{int} \approx \delta_w$. When the wave elevation is small compared with the height of the air boundary layer h_a and with the water depth h_w, the thickness of this region is small, $\delta_{int}/h_a \ll 1$ and $\delta_{int}/h_w \ll 1$, thus making the contribution of the two integrals in (3.6) generally negligible. Furthermore, the assumptions $\delta_{int}/h_a \ll 1$ and $\delta_{int}/h_w \ll 1$, allow us also to introduce a single interface position, $h_{int} \approx h_{int}^{<} \approx h_{int}^{>}$. Hence, the vertical stress balances for small water wave elevations can be finally simplified as

$$\begin{aligned} P &= P_b - \rho_w\langle v'v'\rangle + \rho_w g_2\, \hat{y} && \text{for } \hat{y} < h_{int} \\ P &= P_b - \rho_a\langle v'v'\rangle + g_2 h_{int}\left[\rho_w + \rho_a\left(\frac{\hat{y}}{h_{int}} - 1\right)\right] && \text{for } \hat{y} > h_{int} \end{aligned} \tag{3.7}$$

We address now the behaviour of the total shear stresses that for the present flow symmetries read

$$T_{12} = \langle \tau_{12} \rangle - \langle \rho \, u'' v'' \rangle \tag{3.8}$$

and the stremwise momentum equation (3.2) can be recasted as

$$\frac{dT_{12}}{dy} - \frac{d\langle\rho\rangle \widetilde{u}\,\widetilde{v}}{dy} = \frac{dP_b}{dx} \tag{3.9}$$

that integrates to

$$T_{12} - T_{12}^b - \langle\rho\rangle \widetilde{u}\,\widetilde{v} = \frac{dP_b}{dx}\hat{y} \tag{3.10}$$

where

$$T_{12}^b = \mu_w \frac{dU}{dy} \equiv \rho_w u_{\tau_w}^2 \tag{3.11}$$

is the total shear stress at the water bed $\hat{y} = 0$ that can be used to define the friction velocity at the water bed, $u_{\tau_w}^2$. For $\hat{y} = h_w + h_a$, we have $T_{12} = 0$ and $\langle\rho\rangle \widetilde{u}\,\widetilde{v} = 0$ and equation (3.10) allows us to link the imposed streamwise pressure gradient with the friction velocity at the water bed,

$$T_{12}^b = -H \frac{dP_b}{dx} \equiv \rho_w u_{\tau_w}^2 \tag{3.12}$$

where $H = \big(h_w + h_a\big)$. Hence, the friction velocity at the water bed reads

$$u_{\tau_w} = \sqrt{-\frac{H}{\rho_w}\frac{dP_b}{dx}} \tag{3.13}$$

By considering now $\hat{y} = h_{int}^{>}$, we have again that $\langle\rho\rangle \widetilde{u}\,\widetilde{v} = 0$ and the streamwise stress balance (3.10) reduces to

$$T_{12} = -h_a \frac{dP_b}{dx} \qquad \text{for } \; \hat{y} = h_{int}^{>} \tag{3.14}$$

where equation (3.11) has been used and we have again assumed that $\delta_{int}/h_a \ll 1$ and $\delta_{int}/h_w \ll 1$ thus allowing us to write this approximation $h_{int}^{>} - H \approx -h_a$. From equation (3.14), it is possible to derive an equation for the friction velocity at the top edge of the interface region for $\hat{y} = h_{int}^{>}$. Indeed, at this location, the total shear stress can be recasted as

$$T_{12} = \mu_a \frac{dU}{dy} - \rho_a \langle u'v' \rangle \qquad \text{for } \; \hat{y} = h_{int}^{>} \tag{3.15}$$

that using equation (3.14) allows us to write

$$\mu_a \frac{dU}{dy} = -h_a \frac{dP_b}{dx} + \rho_a \langle u'v' \rangle \qquad \text{for } \; \hat{y} = h_{int}^{>} \tag{3.16}$$

where the viscous term can be used to define the friction velocity for the air boundary layer, i.e.

$$\rho_a u_{\tau_a}^2 \equiv \mu_a \frac{dU}{dy}\bigg|_{\hat{y}=h_{int}^{>}} \tag{3.17}$$

Hence, the friction velocity for the air boundary layer can be then computed as

$$u_{\tau_a} = \sqrt{-\frac{h_a}{\rho_a}\frac{dP_b}{dx} + \langle u'v' \rangle} \tag{3.18}$$

In this region of the flow $\langle u'v' \rangle$ is essentially due to the wave motion and, by assuming again a small wave elevation, it has a negligible contribution. Hence, the friction velocity of the air boundary layer for small water waves can be finally estimated as

$$u_{\tau_a} = \sqrt{-\frac{h_a}{\rho_a}\frac{dP_b}{dx}} \tag{3.19}$$

thus showing the significantly large value attained by the friction velocity for the air flow (indeed turbulent in the present simulation) with respect to that of the water flow (indeed laminar in the present simulation).

It is important now to recall that $\langle \rho \rangle \widetilde{u}\,\widetilde{v} = 0$ in the entire flow except to the thin region $h_{int}^{<} < \hat{y} < h_{int}^{>}$ where the fluid properties change. By assuming that

$$|\langle \rho \rangle \widetilde{u}\,\widetilde{v}| \ll \frac{dP_b}{dx}\hat{y} \tag{3.20}$$

also for $h_{int}^{<} < \hat{y} < h_{int}^{>}$, the contribution to the streamwise stress balance (3.10) of $\langle \rho \rangle \widetilde{u}\,\widetilde{v}$ can be always neglected. The inspection of the data from the present simulation supports this assumption. Hence, from equation (3.10), we can finally write the behaviour of the total shear stresses as,

$$T_{12} = -H\frac{dP_b}{dx}\left(1 - \frac{\hat{y}}{H}\right) \tag{3.21}$$

where again equation (3.11) has been used.

Chapter 4

Mean flow structures

4.1 The structure of water waves

We start the analysis of the Direct Numerical Simulation data by addressing the structure of the developed water waves. Indeed, contrary to several previous attempts where the wave state is essentially prescribed, the water-wave pattern here obtained is the result of the mutual interaction of the turbulent wind with the water surface based on first principles and, hence, it deserves a detailed analysis.

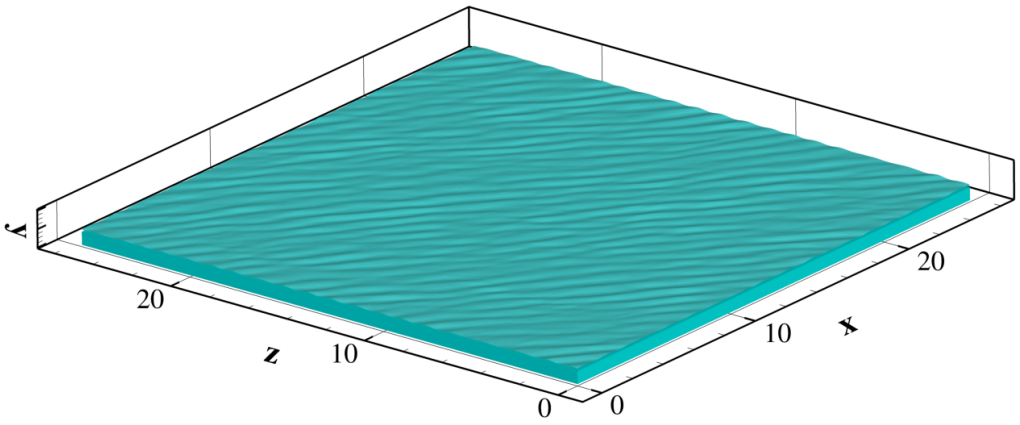

Figure 4.1: Instantaneous water-wave pattern. The vertical wave length has been expanded by a factor 80 for readability reasons.

The instantaneous pattern taken by the water-waves is shown in figure 4.1 by means of an iso-surface of the phase fraction $\alpha = 0.5$. Notice that, for readability reasons, the vertical size of waves has been expanded by a factor of 80. Indeed, the wave height δ_w measured as the difference between the maximum and minimum

water surface elevation is found to be very small compared with both the water depth and with the length scales of the turbulent wind boundary layer,

$$\begin{aligned} \delta_w &= 9.2 \times 10^{-4} \\ \delta_w^+ &= 0.3 \end{aligned} \tag{4.1}$$

where

$$\delta_w = \eta_{max} - \eta_{min} \tag{4.2}$$

with the surface elevation defined as

$$\eta(x, z) = y_\alpha - \langle y_\alpha \rangle \tag{4.3}$$

and $\alpha(x, y_\alpha, z) = 0.5$. Accordingly, also the wave steepness is very small, $S = 7.3 \times 10^{-04}$.

As shown in the previous section §2.2, the flow state is completely determined by the streamwise pressure gradient dP_b/dx and by the ratio between the air and water depths h_a/h_w. A consequence of the measured very small value of the wave height is that we can drop the dependence of the wave state on the ratio h_a/h_w. Let us notice that, due to the use of periodic boundary conditions in the streamwise and spanwise directions, the significant effect that the wind fetch usually has on the water wave state is here avoided being the fetch length formally infinite. In conclusion, the water wave evolution here analysed depends uniquely on the selected value of the streamwise pressure gradient dP_b/dx and, in turn, with the friction Reynolds number of the wind that is completely determined by the pressure gradient itself

$$Re_{\tau_a} \approx \underbrace{\sqrt{-\frac{h_a}{\rho_a}\frac{dP_b}{dx}}}_{u_{\tau_a}} \frac{h_a}{\nu_a} \tag{4.4}$$

It is important to anticipate here that despite the small height of the water waves, their dynamical effect on the statistical features of the turbulent wind boundary layer are far from being negligible as it will be shown in the next sections §4.2, 5 and 5.3.

Surprisingly, figure 4.1 highlights that the water surface develops an oblique water-wave pattern whose inclination with respect to the wind x-direction is $\gamma \approx 38.6°$. It is recognized that according to resonance mechanisms of wind-wave generation (Phillips, 1957), two dominant wave systems propagate at oblique angles symmetric to the wind direction (Morland, 1996). This symmetry is however often broken for moderate winds as demonstrated by several laboratory and field experiments, e.g. Walsh *et al.* (1985, 1989); Caulliez & Collard (1999); Hwang & Wang (2001); Hwang *et al.* (2019); Shemer (2019), reporting asymmetry in the directional spectra at early stages of wind waves evolution.

Interestingly, we also observe that the generated oblique wave pattern propagates at an angle in the upstream direction, i.e. the phase speed vector is aligned with the dominant wavenumber of the water waves with a negative streamwise component. In particular, we measure $\boldsymbol{c}^+ \approx (-10, -8)$. Upwind-traveling waves have been already observed in the past, see e.g. Plant & Wright (1980); Hara & Karachintsev (2003); Wang & Hwang (2004). In accordance with linear perturbation (Plant & Wright, 1980), the dependence of the wave propagation on the wind shear is odd while on the inertial pressure is even. Hence, wind shear can be thought as responsible for a downwind propagation of waves together with a water surface drift while the pressure field can give rise to both upwind and downwind travelling waves. This even effect of pressure is usually broken by the so-called sheltering mechanisms of wind separation over the water surface. However, due to the very low steepness of the present water waves, the wind is able to follow the deformed water surface thus not giving rise to asymmetric pressure distributions in the windward and leeward sides of waves and, hence, we argue that the oblique upwind propagation of waves is essentially induced by the wind pressure field forming on their top. Accordingly, field experiments show that upwind travelling waves occur mostly in open oceans then in sheltered bays as reported by Wang & Hwang (2004).

From a statistical point of view, this oblique water-wave pattern can be characterized quantitatively by addressing the two-point correlation function of the wave elevation,

$$R_{\eta\eta}(r_x, r_z) = \frac{\langle \eta(x + r_x/2, z + r_z/2, t)\eta(x - r_x/2, z - r_z/2, t)\rangle}{\langle \eta^2 \rangle} \,. \tag{4.5}$$

As shown in figure 4.2, the two-point correlation function exhibits an inclined ($\gamma \approx 38.6°$) oscillatory behaviour typical of quasi-periodic phenomena. The distance from the origin of the first positive peak in the correlation along the direction normal to the wave pattern can be used to measure the characteristic wave length. We measure $\lambda^+ = 296$. The projection in the streamwise and spanwise directions of this typical wave length is useful for the forthcoming analysis and is measured to be $(\lambda_x^+, \lambda_z^+) = (475, 380)$. On the other hand, by rescaling the wave length with the water depth, we measure $\lambda/h_w = 1.55$ thus highlighting a deep water regime. This observation further support the previous assumption that, in the present flow settings, the flow state is primarily driven by the imposed pressure gradient dP_b/dx with a substantial weak dependence on the water depth h_w.

The two-point spatial correlation function (4.5) can now be used to compute the one-dimensional spectrum of the wave elevation,

$$\begin{aligned} \hat{E}^x_{\eta\eta}(k_x) &= \mathcal{F}\left\{R_{\eta\eta}(r_x, 0)\right\} \\ \hat{E}^z_{\eta\eta}(k_z) &= \mathcal{F}\left\{R_{\eta\eta}(0, r_z)\right\} \end{aligned} \tag{4.6}$$

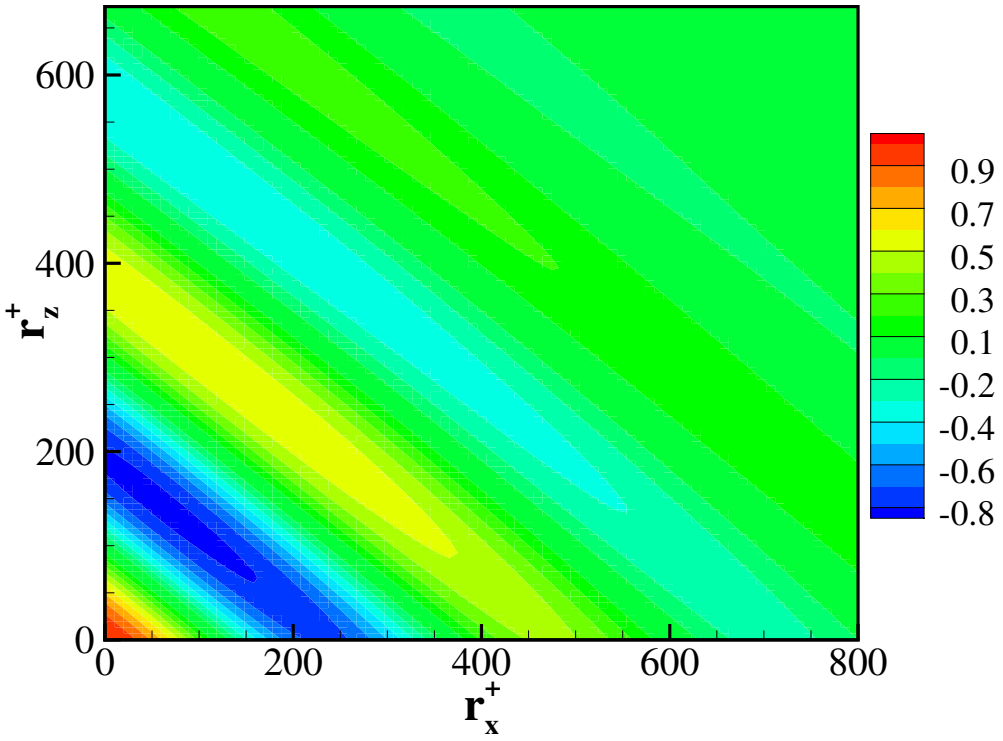

Figure 4.2: Two-point spatial correlation function of the wave elevation $R_{\eta\eta}(r_x, r_z)$.

where the operator $\mathcal{F}$ denotes the Fourier transform. The one-dimensional spectrum allows us to identify the scales of the most intense waves. As shown in figure 4.3, both the streamwise and spanwise wave elevation spectra highlight a peak of intensity that is located at streamwise and spanwise wavenumbers that are of the same order of the wavelengths previously measured with the two-point correlation, i.e. $\lambda^+_{x,peak} = 2\pi/k^+_{x,peak} = 450$ ($k^+_{x,peak} = 1.39 \times 10^{-2}$) and $\lambda^+_{z,peak} = 2\pi/k^+_{z,peak} = 386$ ($k^+_{z,peak} = 1.63 \times 10^{-2}$). Two relevant additional statistical features are however evident. The first is given by the presence of a broad range of wavenumbers where the intensity of the wave elevation is not negligible thus highlighting the occurrence of a multi-scale interface typical of realistic water surfaces. The second is given by the appearance of a secondary peak in the streamwise spectrum at small wavenumbers, $k^+_x = 3.1 \times 10^{-3}$, corresponding to a wavelength $\lambda^+_{x,peak} = 2\pi/k^+_{x,peak} = 2026$. This secondary peak is a statistical footprint of the presence of group waves typical of deep water. Hence, the oblique water-wave pattern analysed so far turns out to be superimposed to a longer wave envelop developing in the streamwise direction.

It is possible now to address some classical parameters used to characterize the

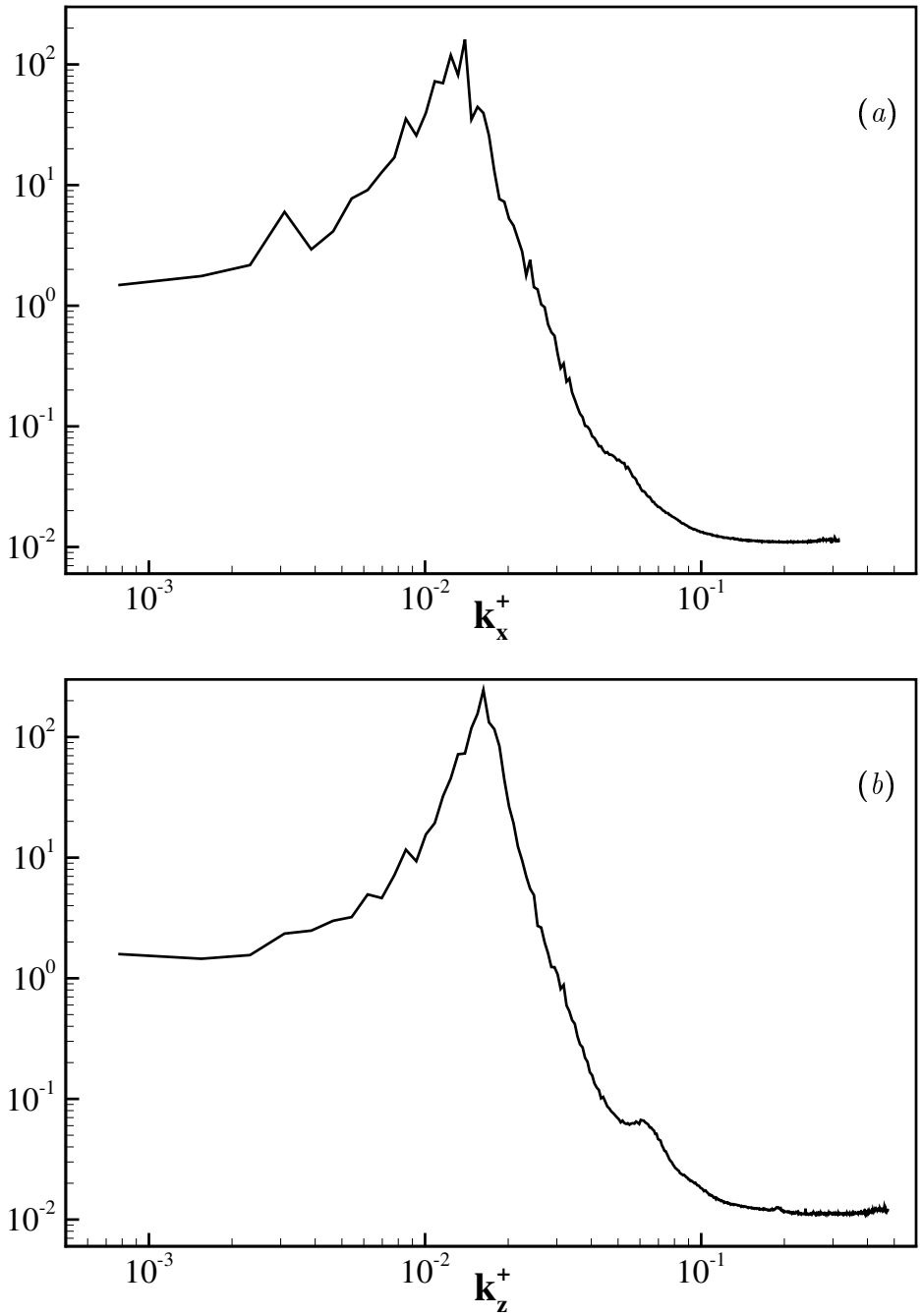

Figure 4.3: Streamwise (a) and spanwise (b) one-dimensional spectrum of the wave elevation $\hat{E}^x_{\eta\eta}$ and $\hat{E}^z_{\eta\eta}$, respectively.

state of water waves. Of particular interest is the so-called Bond number,

$$Bo = \frac{\sigma(2\pi/\lambda)^2}{\rho_w g} \tag{4.7}$$

that is a measure of the major restoring force between gravity and surface tension. In the present simulation we measure $Bo \approx 5.1 \times 10^{-3}$ thus suggesting that the developed waves can be classified as gravity waves.

In closing this section, let us remind that the here described water wave field is the result of a fully coupled, first principle, evolution of a turbulent wind over a water surface where the unique control parameter is the pressure gradient dP_b/dx and, hence, the friction Reynolds number Re_{τ_a} of the wind being the effect of water depth negligible in accordance with the previously shown deep water regime and because the wind fetch length is formally infinite. Accordingly, we may conclude that for a friction Reynolds number $Re_{\tau_a} = 317$, the wind-wave interaction problem develops a wave pattern propagating at an angle in the upwind direction of deep water gravity waves at very low wave steepness and elevation.

4.2 The structure of the turbulent wind

We consider now the behaviour of the wind turbulent boundary layer. Let us recall that the stresses at the water surface created by the wind are responsible for the formation of the previously analysed water-wave pattern that in turn influences the wind boundary layer thus forming a complex fully coupled mechanisms. Hence, it is very relevant now to address how the physical properties of the turbulent wind are different with respect to classical behaviours observed in wall-bounded boundary layer.

4.2.1 Turbulent coherent motions

In this section we start the study of the turbulent wind by addressing the topology of the turbulent structures populating it. From an instantaneous point of view, coherent vortical structures can be identified by using the so-called λ_2 criterion(Jeong *et al.*, 1997) where λ_2 is the second largest eigenvalue of the tensor

$$S_{ik}S_{kj} + \Omega_{ik}\Omega_{kj} \tag{4.8}$$

where $S_{ij} = (\partial u_i/\partial x_j + \partial u_j/\partial x_i)/2$ and $\Omega_{ij} = (\partial u_i/\partial x_j - \partial u_j/\partial x_i)/2$ are the symmetric and antisymmetric parts of the velocity gradient tensor. In figure 4.4 the isosurface of $\lambda_2 = -3$ colored with the streamwise velocity is shown. Figure 4.4 shows that quasi-streamwise vortices are the dominant vortical structure above the wave

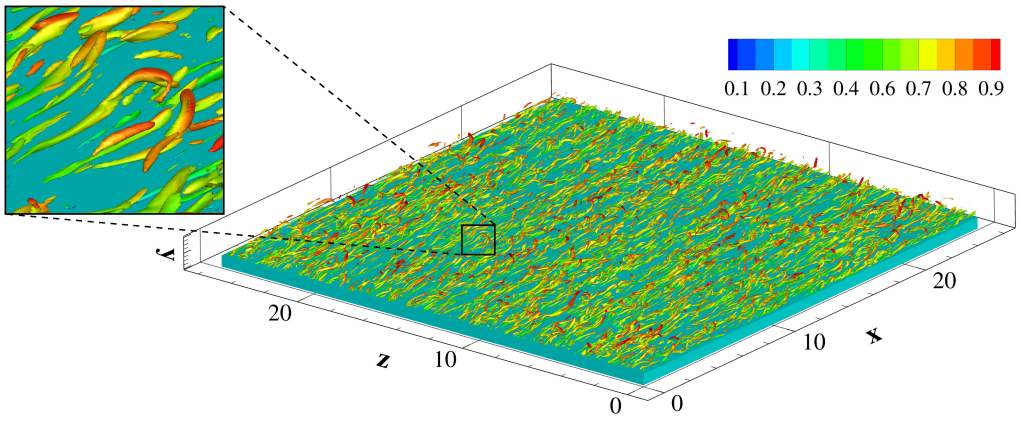

Figure 4.4: Instantaneous vortex pattern in the turbulent wind boundary layer shown by means of an iso-surface of $\lambda_2 = -3$ colored with the streamwise velocity.

surface. Consistently with the low elevation and steepness of the water wave pattern described in the previous section 4.1, the evolution of the observed quasi-streamwise vortices is essentially not constrained by the water-wave pattern, thus leading to a vortex dynamic that resembles the one commonly observed in wall-bounded turbulence. Such turbulent structures by interacting with the mean velocity gradient are known to give rise to streamwise velocity streaks as a result of ejection and sweeping of fluid from/to the near-interface region.

In order to give a quantitative description of these wind boundary layer structures and to highlight their statistical relevance, we consider the two-point spatial autocorrelation function of the velocity field,

$$R_{u_i u_i}(\boldsymbol{x}, \boldsymbol{r}) = \frac{\langle u_i'(\boldsymbol{x} + \boldsymbol{r}, t) u_i'(\boldsymbol{x}, t) \rangle}{\langle u_i' u_i' \rangle (\boldsymbol{x})} \tag{4.9}$$

where no summation is implied for index i. As shown in figure 4.5(a), the streamwise correlation function evaluated at $y^+ = 30$ shows that all the three velocity components are correlated over relatively long distances. In particular, we measure a correlation length $\ell^+_{corr_x} \approx 1250$ and $\ell^+_{corr_x} \approx 700$ for the vertical and spanwise velocity components, respectively, while $\ell^+_{corr_x} \approx 2800$ for the streamwise one. Here, the correlation length is measured as the spatial increment where $R_{u_i u_i} = 0.05$. These values significantly exceed those commonly reported for wall-bounded turbulence thus highlighting an elongation of the turbulent structures due to the presence of the water-wave surface. The correlation function in the spanwise direction is shown in figure 4.5(b). In this case, negative peaks of correlation are observed for the streamwise and vertical velocity components that can be understood as a clear statistical evidence of the presence of high and low streamwise velocity streaks and

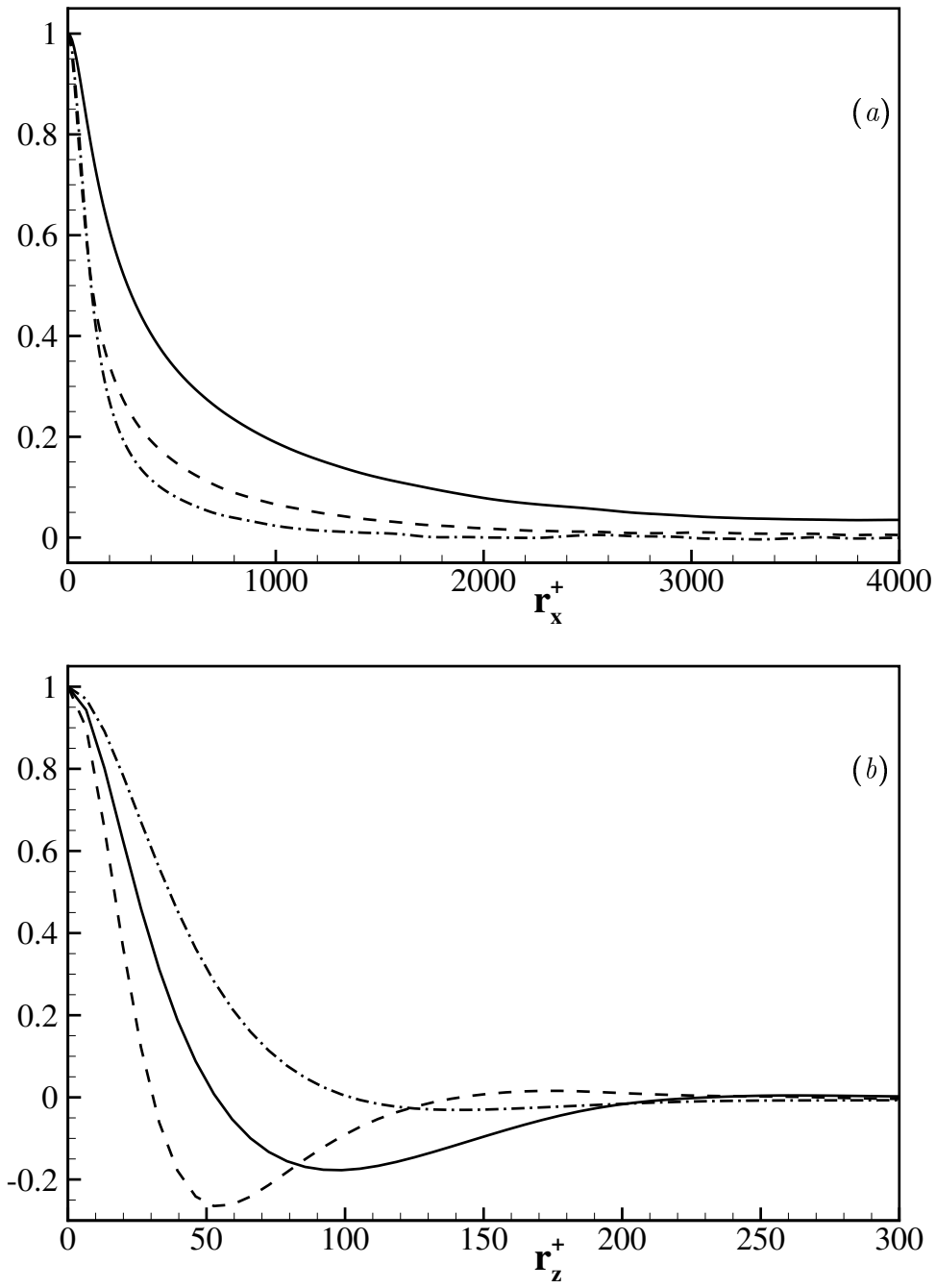

Figure 4.5: Two-point spatial auto-correlation function of the velocity field $R_{u_i u_i}$ computed in the buffer layer region at $y^+ = 30$. (a) Streamwise correlation for $r_y = r_z = 0$. (b) Spanwise correlation for $r_x = r_y = 0$. R_{uu} (solid line), R_{vv} (dashed line) and R_{ww} (dashed dotted line)

of quasi-streamwise vortices, respectively. In particular, the value of the spanwise scale r_z where these negative peaks occur can be used as a measure of their spanwise size. Accordingly, we measure a spanwise spacing between streamwise velocity streaks of $r_z^+ \approx 100$ (location of the negative peak of R_{uu}) and a spanwise size of quasi-streamwise vortices of $r_z^+ \approx 53$ (location of the negative peak of R_{vv}). Also in this case, these values are significantly larger than those commonly observed in wall turbulence where the spacing between streamwise velocity streaks and the diameter of quasi-streamwise vortices are measured to be of the order of $r_z^+ \approx 50$ and $r_z^+ \approx 30$, respectively (Kim *et al.*, 1987; Abe *et al.*, 2001). In conclusion, the topology of turbulent structures responsible for the self-sustaining mechanisms of turbulence in the the wind boundary layer essentially resembles that observed in classical wall-turbulence. The main difference is indeed only of quantitative nature being the size of the turbulent structures resulting from wind-wave interactions quite larger than those observed in wall-bounded flows. This similarity with wall turbulence is not maintained in the very-near interface region. There, the effect of the presence of a wind-induced water wave pattern becomes significant giving rise to peculiar ordered motions related with the presence wind-wave interaction phenomena as it will be shown in the next section 4.2.2.

4.2.2 Wave-induced Stokes sublayer and interface stresses

The oblique wave pattern analysed in section 4.1 is responsible for the appearance of a very interesting phenomenon in the very near-interface region of the wind boundary layer. Indeed, it is possible to assume that the air flow, when interacting with the water wave field, it accelerates on the windward side and then decelerates on the leeward side. This behaviour can be associated with a pattern for the pressure field that is minimum above the wave crests and maximum within the trough region. As shown in figure 4.6(a), the instantaneous pressure field actually confirms this scenario by reproducing a pattern that conforms with that of the wave elevation that is reported for comparison in figure 4.6(b). Because the water wave pattern is skewed with respect to the mean wind direction, these pressure variations give rise to periodically distributed pressure gradients in both the streamwise and spanwise directions. Of particular interest is the effect of the latter gradient that is responsible for the generation of an oscillating spanwise forcing thus inducing an alternating spanwise motion, as shown in figure 4.7(a). The relevance of this observation is given by the fact that this near-interface velocity pattern emulates the flow behaviour of the so-called *generalized Stokes layer* that is widely recognize to reduce the levels of drag in wall-bounded turbulence (Quadrio *et al.*, 2009; Quadrio & Ricco, 2011). As it will be shown in the next section 5, also the present turbulent wind, by interacting with the water wave field, is characterized by a significant reduction of drag with respect to wall-bounded turbulence. It is then possible to conjecture that this drag

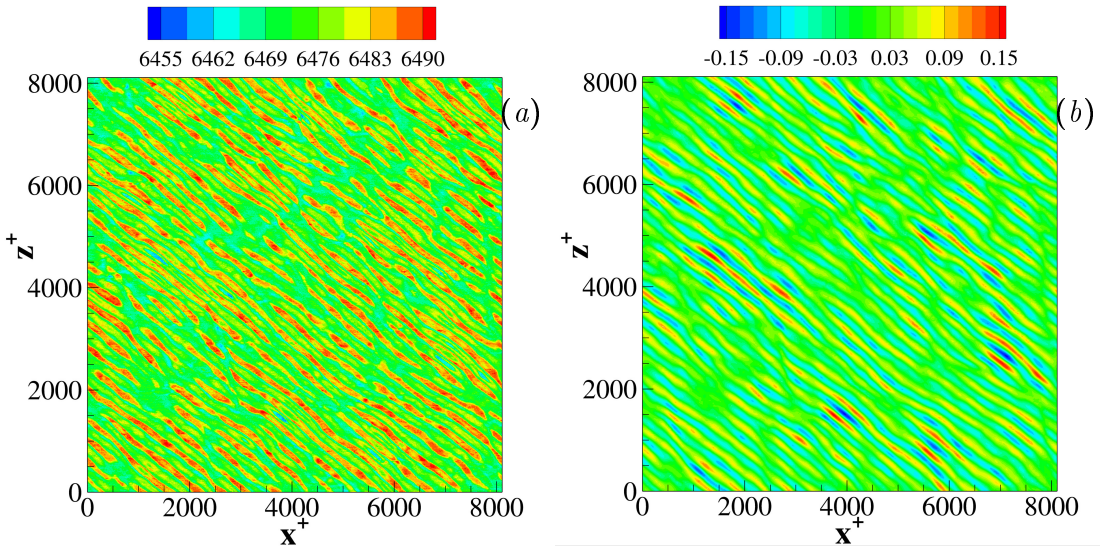

Figure 4.6: Iso-contours of the instantaneous pressure field $p^+(x,z)$ (a) and wave elevation $\eta^+(x,z)$ (b) both evaluated at the water interface $\alpha = 0.5$.

reduction is related with the presence of a spanwise oscillating motion induced by the presence of a skewed wave pattern in analogy with the results obtained in Ghebali *et al.* (2017) using skewed wavy walls. For this reason, a deeper analysis of the very near-interface region and of the *wave-induced Stokes sublayer*, is here reported.

In contrast with the generalized Stokes layer reproduced by the spanwise wall motion in active control techniques, the velocity field in the wind-wave case periodically accelerate/decelerate also in the streamwise and vertical direction as a result of the pressure field pattern previously analysed and shown in figure 4.6(a). However, it is not the velocity field but the associated shear stresses at a certain location within the boundary layer that is known to be responsible for the weaken of turbulence and, hence, for the consequent drag reduction (Touber & Leschziner, 2012). As shown in figure 4.7(b) the instantaneous spanwise shear $\partial w/\partial y$ at the water surface exhibits an alternating positive and negative behaviour respectively at the wave crest and trough region. The apparent irregularity of this behaviour is clear footprint at the water surface of the stresses induced by streamwise-aligned turbulent structures that have been shown in the previous section 4.2.1 to dominate the wind boundary layer further away from the water surface.

To clear the analysis of the generalized Stokes sublayer of wind-wave flows from the effects of turbulence structures above it, we introduce here a conditional average procedure to address the very-near interface behaviour separately on the crest and trough wave regions. For the generic quantity β, two conditional averages, denoted as $\langle\beta\rangle_\cap$ and $\langle\beta\rangle_\cup$, are computed as the average over (x,z) points that satisfy the

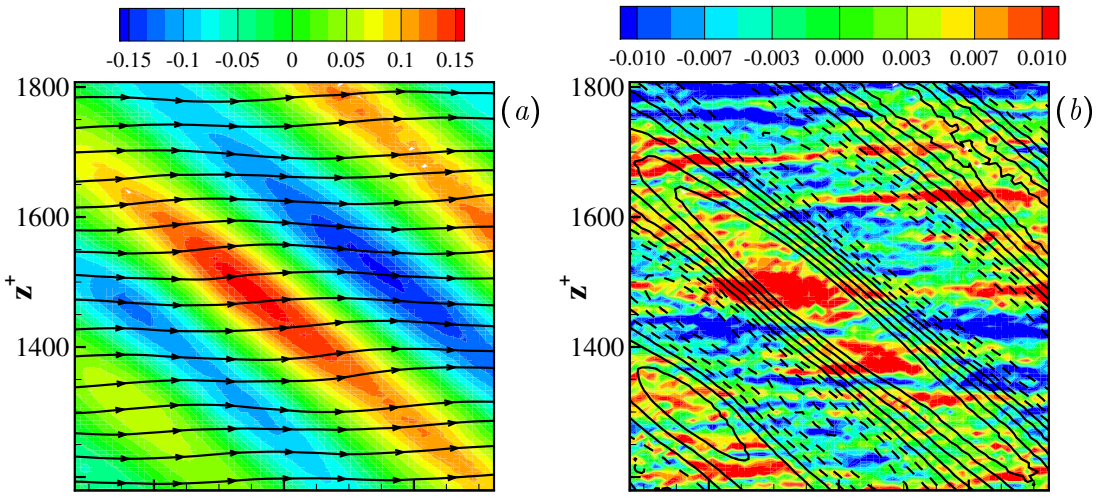

Figure 4.7: (a) Iso-contours of the instantaneous wave elevation $\eta^+(x,z)$ and velocity field streamlines. (b) Iso-contrours of the instantaneous spanwise shear $\partial w^+/\partial y^+(x,z)$ superimposed to the iso-levels of the wave elevation $\eta^+(x,z)$ where positive and negative values are reported with solid and dashed lines, respectively. Both panels show a portion of the entire domain in order to improve the readability of the behaviour by enlarging the view.

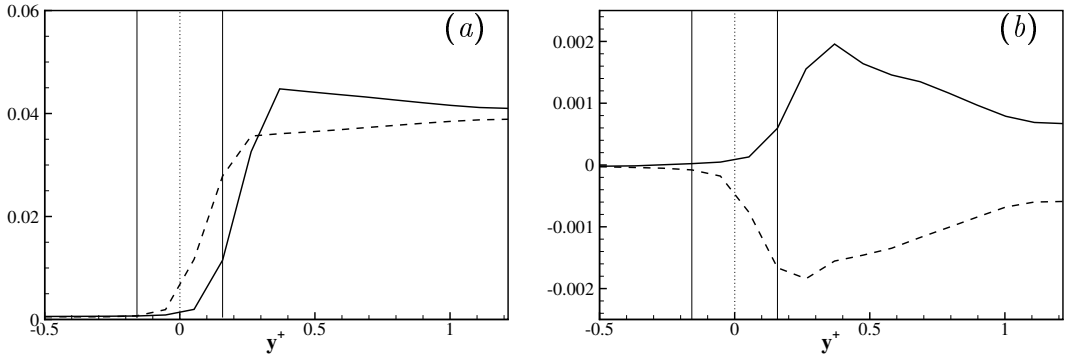

Figure 4.8: Very-near interface behaviour of the crest and trough conditional averages of (a) streamwise shear, $\langle \partial u/\partial y \rangle_{\cap}^{+}$ (solid line) and $\langle \partial u/\partial y \rangle_{\cup}^{+}$ (dashed line), respectively and of (b) spanwise shear $\langle \partial w/\partial y \rangle_{\cap}^{+}$ (solid line) and $\langle \partial w/\partial y \rangle_{\cup}^{+}$ (dashed line), respectively. The vertical solid lines denote the average position of the wave crest and trough.

conditions $\eta(x,y,z,t) > 0.7\,\delta_w/2$ (crests) and $\eta(x,y,z,t) < -0.7\,\delta_w/2$ (trough), respectively. As shown in figure 4.8(a), the flow in the very near-interface region is characterized by higher streamwise velocity gradients in the crest rather than in the trough regions in accordance with the pressure field pattern induced by the water wave field analysed so far. In accordance with this wave-induced pressure field and as shown in figure 4.8(b), the mean spanwise velocity gradient exhibits a reverse of sign moving from the crest to the trough regions. Interestingly, the peaks of streamwise and spanwise shear are not located at the water surface but slightly away from it. This behaviour is related with the interaction of the water surface that, contrary to the generalized Stokes layer induced by moving walls, forms an accelerating/decelerating wave pattern based on first principles. We measure that for the wave-induced Stokes sublayer, the peak of spanwise shear stresses is reached at $y^+ \approx 0.4$ on the wave crests and at $y^+ \approx 0.25$ on the trough regions. By recalling that the maximum and minimum average values of the wave elevations are $\eta^+_{max} \approx 0.15$ and $\eta^+_{min} \approx -0.15$, we can conclude that these peak values are further away from the water surface in the trough regions than in the wave crests, see the vertical lines in figure 4.8(b).

In closing this section, let us point out that in drag reducing techniques based on oscillating walls, the thickness of the Stokes layer has been recognized as an important quantity for the effectiveness of the viscous shearing action of the moving wall to weaken the near-wall turbulence interactions (Quadrio & Ricco, 2011). For the present wave-induced Stokes sublayer, we measure a penetration length $\ell_S^+ \approx 2$, computed as the interface distance where the conditionally averaged spanwise shear reaches 10% its maximum. This value is compatible with a drag reduction state

of the wind boundary layer in accordance with Quadrio & Ricco (2011) where the minimal condition for drag reduction has been found to be $\ell_S^+ \approx 1$.

To summarize, the near interface field highlights the presence of a wave-induced Stokes sublayer similar to that observed in Ghebali *et al.* (2017) for solid skewed wavy walls. The relevance of this layer for the turbulent wind flowing above it is recognized to be in the associated oscillating spanwise motion. The resulting field of spanwise shear takes the form of a streamwise travelling wave whose wavelength and phase speed is the one of the water waves, i.e. $\lambda_x^+ \approx 475$ and $c_x^+ \approx -10$. The intensity of the associated motion and its region of influence are small, $|w|_{max}^+ \approx 10^{-3}$ and $\ell_s^+ \approx 2$, but as shown in the following section 5, their effects on the wind boundary layer are not being responsible for a non-negligible drag reduction.

Chapter 5

Mean wind profiles

The present simulation highlights that the mutual interaction of a water surface with a turbulent wind at a friction Reynolds number $Re_{\tau_a} = 317$ leads to a skewed pattern of low steepness waves as shown in section 4.1. This field of water waves modifies the structure of the turbulent wind as shown in section 4.2 that in turn created them thus forming a complex self-sustaining mechanism. Accordingly, it is now relevant to study how and to what degree, the statistical features of the turbulent wind are affected by this modified structures with respect to classical behaviours of wall turbulence.

5.1 Mean flow

The effect of moving water waves on the mean wind profile is of overwhelming interest for wind-wave problems in general. In the present flow settings, the interaction of wind with moving waves creates a wave-induced Stokes sublayer which modulates the near-surface flow. It is then important to address if this near-surface modulation affects also the wind flow further away from the water surface thus leading to a departure from the mean velocity logarithmic law classically observed in wall turbulence. To this aim, we compare the mean velocity profiles from our simulation with those from the Direct Numerical Simulation of an open channel at $Re_\tau = 300$ performed by Nagaosa & Handler (2003).

Before that, let us point out that the time variation of the wave state makes essential to define a method to capture the origin of the wind turbulent boundary layer. In analogy with wall turbulence, we localize the virtual origin in correspondence of the maximum of the mean velocity gradient. The resulting location is $y_0^+ = 0.37$, i.e. slightly above the water wave pattern, and the corresponding mean velocity is $U_0^+ = 0.75$. Following this criterion the mean velocity profile will be shown by re-scaling the velocity and the vertical coordinate with U_0 and y_0, respectively.

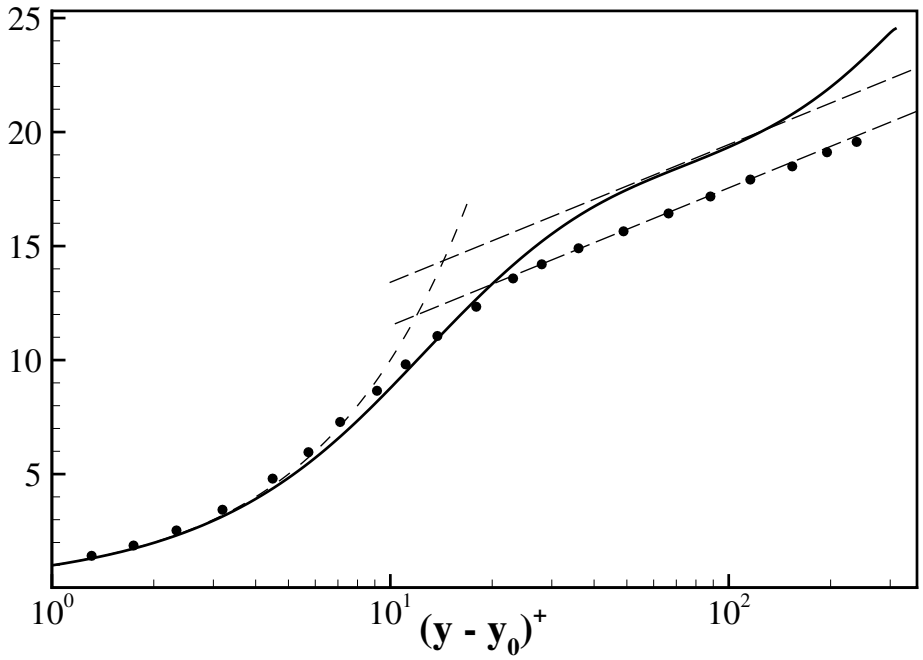

Figure 5.1: Mean wind velocity profile $(U - U_0)^+$ (solid line) compared with the mean velocity profile of wall turbulence in a open channel (Nagaosa & Handler, 2003) (filled circles). The linear law and interpolating logarithmic laws are shown with dashed lines.

As shown in figure 5.1, the mean velocity profile is found to follow the classical scalings of the viscous sublayer for $(y-y_0)^+ < 5$ and of the buffer layer for $(y-y_0)^+ < 20$. However, for $(y-y_0)^+ > 20$ the mean velocity profile is found to deviate from the classical scalings of wall turbulence especially in the overlap and outer layers. It consists of an upward shift of the mean velocity field with respect to that obtained from wall turbulence in a open channel. This behaviour is consistent with a significant drag reduction of the wind-wave boundary layer with respect to turbulence over smooth walls. Arguably, this phenomenon of drag reduction can be associated with the presence of a wave-induced Stokes sublayer that, in turbulence control techniques, is widely recognized to induce a significant drag reduction. In a more quantitative point of view, by assuming a logarithmic behaviour in the putative overlap layer for $30 < (y-y_0)^+ < 0.3Re_\tau$,

$$U^+ - U_0^+ = \frac{1}{\kappa}\log\left(y^+ - y_0^+\right) + B \tag{5.1}$$

we measure a small variation of the von Kármán constant, $\kappa = 0.38$ for the wind-wave problem with respect to $\kappa_{oc} = 0.39$ for wall turbulence in a open channel. On the other hand, the additive constant B is found to substantially increase, $B = 7.3$ for the wind-wave problem with respect to $B_{oc} = 5.7$ for wall turbulence. Hence, the additive constant increment, $\Delta B = B - B_{oc}$, can be understood as a measure of the drag reduction experienced by the wind-wave problem with respect to wall turbulence.

By considering the water wave pattern as rough surface for the wind boundary layer, we can rewrite the logarithmic law for the mean velocity profile as

$$U^+ - U_0^+ = \frac{1}{\kappa}\log\left(\frac{y^+ - y_0^+}{k_s^+}\right) + B_{oc} \tag{5.2}$$

where k_s^+ is an estimate of the surface roughness length by assuming that the upward shift of the mean velocity profile ΔB can be modelled as (Pope, 2000)

$$\Delta B = -\frac{1}{\kappa}\log\left(k_s^+\right) \tag{5.3}$$

Accordingly, the effective roughness length of the water surface that is felt by the mean wind boundary layer can be measured as

$$k_s^+ = e^{-\kappa\Delta B} = 0.54 \tag{5.4}$$

that is of the same order of the mean wave height here measured (4.1).

5.2 Turbulent intensity profiles

The influence of moving surface waves is also visible in the turbulent intensity profiles as shown in figure 5.2. Compared to wall turbulence, the peak intensity of the streamwise velocity fluctuations is significantly higher and shifted towards the wind boundary layer core. Also the peak intensity of the spanwise and vertical velocity fluctuations is moved outward but, in this case, its magnitude is decreased with respect to wall turbulence. The outward shift of the peaks of turbulent activities is in line with many observations in drag reducing flows. The modulation of turbulence given by the wave-induced Stokes layer is such that turbulence is weaken in the very-near interface region. As a consequence, the turbulence self-sustainment mechanisms through which quasi-streamwise vortices and streaks are generated, are moved outward. Indeed, such processes are known to form an autonomous regeneration cycle (Jimenez & Pinelli, 1999) where the presence of the water interface appears to be only necessary to sustain the mean shear. This outward shift allows for the generation of wider and longer velocity streaks as demonstrated by the two-point correlation function reported in section 4.2.1. This scenario is consistent with the increase of the streamwise velocity fluctuation intensity and to the weakening of the spanwise and vertical velocity fluctuations in the very near-interface region shown in figure 5.2.

Analogous considerations can be done for the Reynolds shear stresses shown in figure 5.3. The magnitude of $-\langle u'v' \rangle$ is reduced and its maximum value is reached for a larger value of y^+ with respect to wall turbulence. Interestingly, a change of sign of the Reynolds shear stresses is observed for $y^+ < 1$ as shown in the inset zoom of figure 5.3. This region of the flow represents the wind layer directly affected by the water surface pattern being the wave elevation of the order of $\delta_w^+ = 0.3$ as shown in section §4.1. Indeed, this change of sign is a clear wave-induced effect. Due to the very low steepness of the water waves ($S = 7.3 \times 10^{-04}$), the wind is able to remain attached to the water surface, i.e. wind-wave sheltering mechanisms are absent (Jeffreys, 1925). Accordingly, in the windward side the flow while raising ($v' > 0$) accelerates in the streamwise direction ($u' > 0$). On the contrary, in the leeward side the flow while descending ($v' < 0$) decelerates in the streamwise direction ($u' < 0$). Hence, both the windward and leeward sides contribute to the production of negative Reynolds shear stresses $-\langle u'v' \rangle < 0$. Accordingly to our data, this effect is felt by the wind up to $y^+ = 1$ thus suggesting a penetration length of the wave-induced motions significantly higher than the wave height δ_w itself. This penetration length is of the same order of that of the wind-induced Stokes sublayer $\ell_s^+ \approx 2$ thus suggesting the effectiveness of the resulting spanwise oscillating motion in altering the turbulent dynamics of the wind boundary layer.

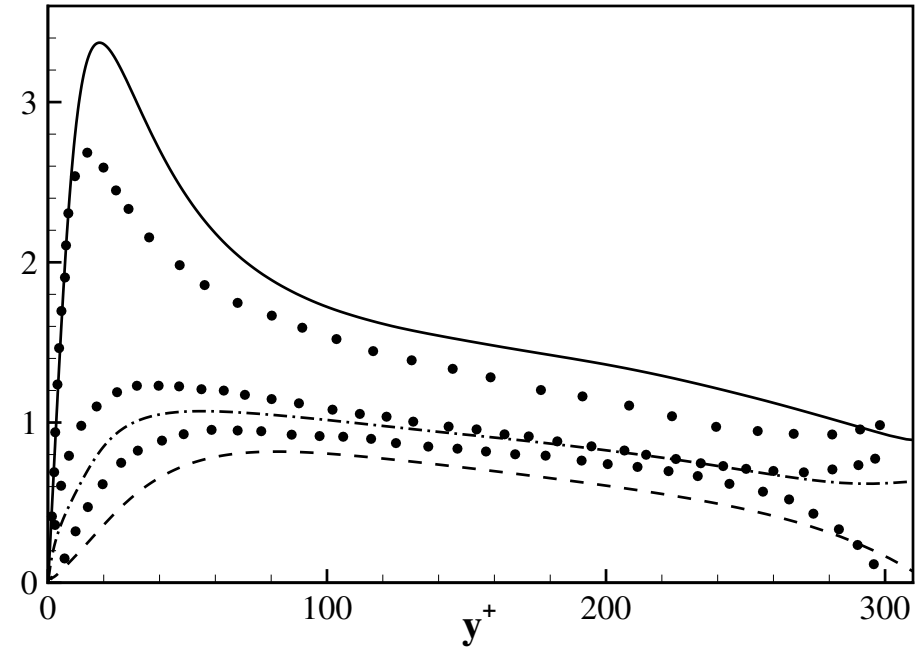

Figure 5.2: Profiles of wind turbulence intensities (lines) compared with the turbulence intensity profiles of wall turbulence in a open channel (Nagaosa & Handler, 2003) (circles). Streamwise turbulent fluctuations $\sqrt{\langle u'u' \rangle}$ (solid line), spanwise turbulent fluctuations $\sqrt{\langle w'w' \rangle}$ (dashed dotted line) and vertical turbulent fluctuations $\sqrt{\langle v'v' \rangle}$ (dashed line).

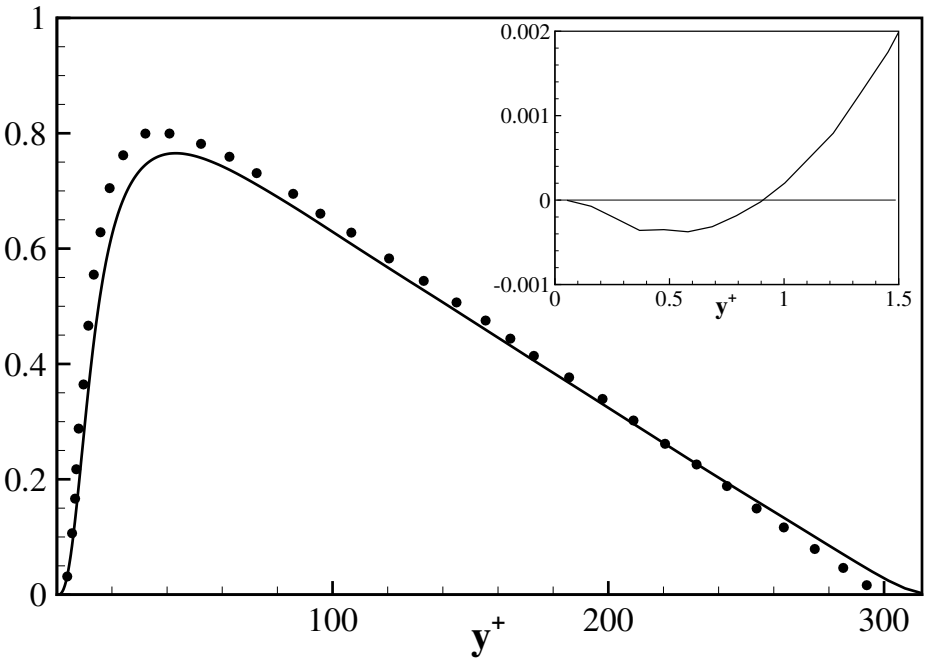

Figure 5.3: Reynolds shear stress $-\langle u'v' \rangle$ profiles in the wind-wave problem (solid line) compared with those of wall turbulence in a open channel (Nagaosa & Handler, 2003) (filled circles). The inset shows an enlargement view of the near-interface region.

5.3 Wind-wave induced field of stresses

Until now, we have addressed the effect of wind-wave interactions on the turbulent wind motions. It is however important also to address the field of stresses induced by wind-wave mechanisms. In particular, it is relevant to establish how and to what extent the related field of stresses penetrate into the wind boundary layer. To this aim, we consider the two-point spatial correlation function of the pressure and Reynolds shear stresses,

$$R_{pp}(\boldsymbol{x},\boldsymbol{r}) = \frac{\langle p'(\boldsymbol{x}+\boldsymbol{r},t)p'(\boldsymbol{x},t)\rangle}{\langle p'p'\rangle(\boldsymbol{x})} \tag{5.5}$$

and

$$R_{uv}(\boldsymbol{x},\boldsymbol{r}) = \frac{\langle u'(\boldsymbol{x}+\boldsymbol{r},t)v'(\boldsymbol{x},t)\rangle}{\sqrt{\langle u'u'\rangle(\boldsymbol{x})}\sqrt{\langle v'v'\rangle(\boldsymbol{x})}} \tag{5.6}$$

respectively.

As shown in figure 5.4, the pressure footprint of the wind-wave interaction mechanisms is felt by the wind boundary layer up to $y^+ \approx 60$. It consists of an oscillating behaviour of the two-point pressure correlation. The clear matching of scales between the water wave lengths $(\lambda_x^+, \lambda_z^+) = (475, 380)$ measured in section §4.1 and the second peak of pressure correlation, clearly suggests that the high and low pressure field pattern induced by water waves at their trough and crest, see figure 4.6, significantly penetrates the wind boundary layer thus affecting its evolution. It is worth remarking the strongly non-local feature of the pressure field that enables long-distance interactions between a very thin layer of water waves, $\delta_w^+ = 0.3$ thick, with the flow structures populating the wind boundary layer core.

Contrary to pressure, the turbulent shear stress footprint of the wind-wave interactions does not significantly penetrate into the wind boundary layer and remains more confined in the near interface region. Indeed, as shown in figure 5.5, the two-point correlation of Reynolds stresses is clearly affected by wind-wave interactions up to $y^+ \approx 3$ while for $y^+ > 3$ the classical behaviour induced by the structures composing the self-sustaining mechanisms of turbulence is observed, i.e. a negative peak in the spanwise correlation function induced by quasi-streamwise vortices and streaks at increasingly larger scales by augmenting the distance from the interface.

Due to the very low steepness of water waves, the wind boundary layer remains attached to water surface and, hence, in the windward side the flow accelerates ($u' > 0$ and $v' > 0$) while in the leeward side the flow decelerates ($u' < 0$ and $v' < 0$) in accordance with the near-interface change of sign of the Reynolds shear stresses shown in the previous section §5.2. Accordingly, we may expect a wind-wave footprint in the two-point correlation in the form of a peak of anti-correlation at half water wave length and a second peak of correlation at the water wave length

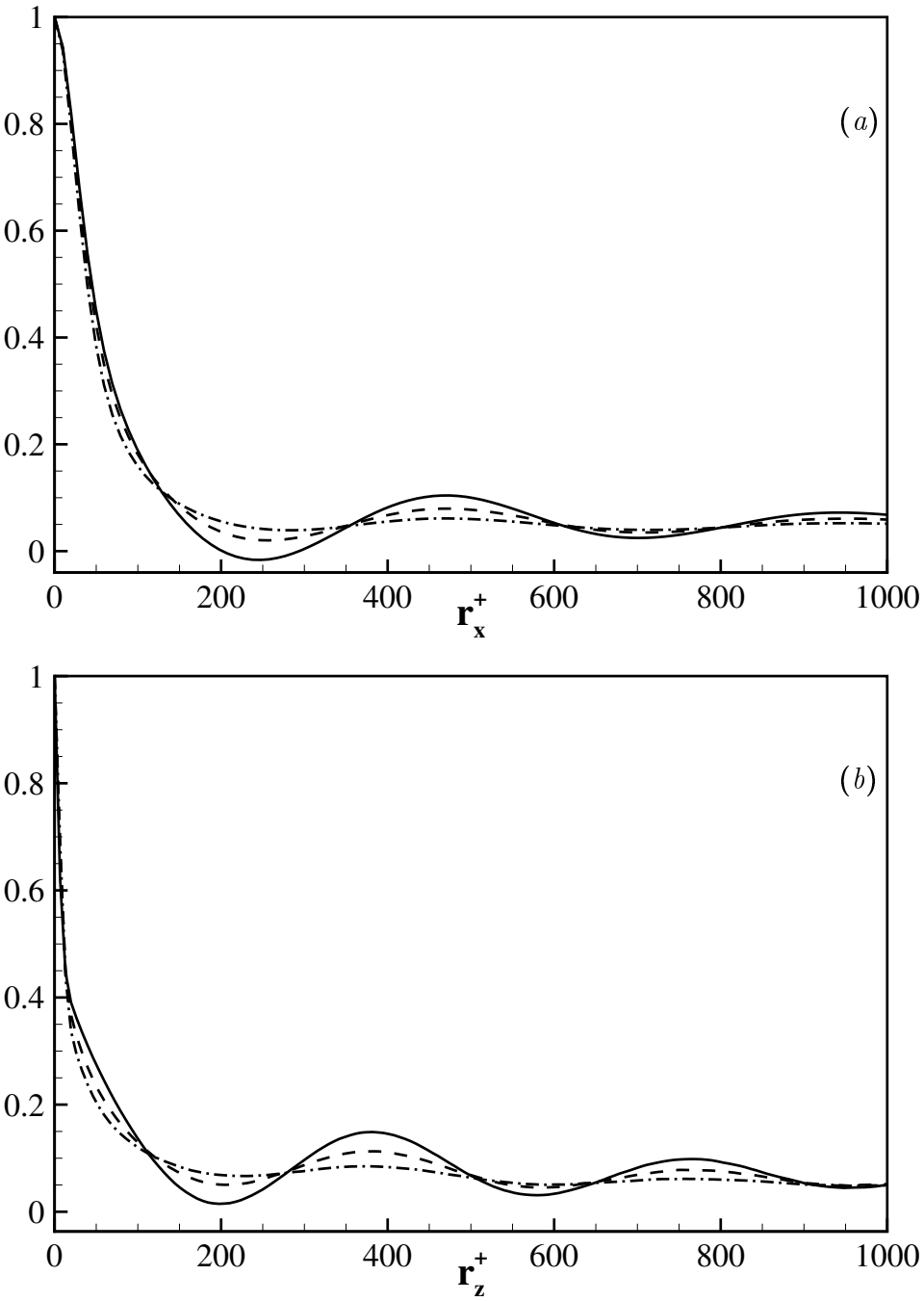

Figure 5.4: Two-point spatial auto-correlation function of the pressure field R_{pp} computed at increasing vertical positions, $y^+ = 15$ (solid line), $y^+ = 30$ (dashed line) and $y^+ = 45$ (dashed dotted line). (a) Streamwise correlation for $r_y = r_z = 0$. (b) Spanwise correlation for $r_x = r_y = 0$.

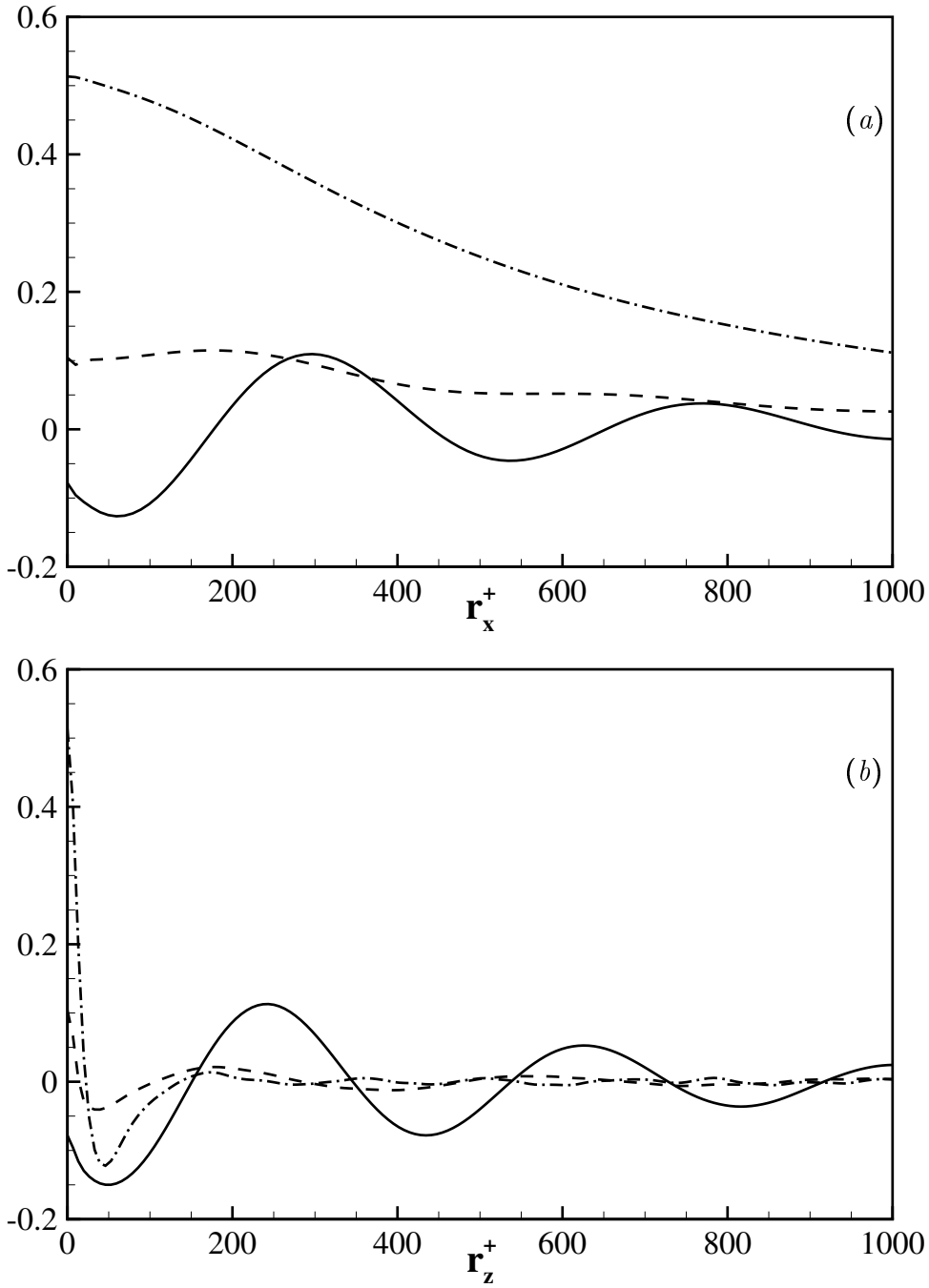

Figure 5.5: Two-point spatial correlation function of the Reynolds shear stresses R_{uv} computed at increasing vertical positions, $y^+ = 0.6$ (solid line), $y^+ = 1.37$ (dashed line) and $y^+ = 5.37$ (dashed dotted line). (a) Streamwise correlation for $r_y = r_z = 0$. (b) Spanwise correlation for $r_x = r_y = 0$.

itself. Figure 5.5 actually confirm this scenario up to $y^+ \approx 3$. The clear matching of scales suggests that this region of influence is governed by the wave-induced Stokes sublayer that has been found to have a penetration length of the same order, $\ell_S^+ \approx 2$.

The two-point correlation function of Reynolds shear stresses highlights another interesting wind-wave feature. Indeed, the peak of correlation for $y^+ < 3$ occurs for non-zero displacements $(r_x, r_z) = (47, 40)$. This is a clear measure of the phase shift between the streamwise acceleretion/deceleration of the flow ($u' > 0$ and $u' < 0$) with respect to the windward raising and leeward descending ($v' > 0$ and $v' < 0$) wave-induced motions. This measured values of shift are of the order of 1/10 the water wave lengths in accordance with measurements performed by Ghebali *et al.* (2017) for solid skewed wavy walls.

Chapter 6

Turbulent kinetic energy budget

For inhomogeneous turbulence, the evolution of the turbulent kinetic energy budget is mandatory to obtain a detailed analysis of one-point statistics such production, dissipation and spatial redistribution of turbulent kinetic energy in the physical space. The intensity of turbulence in a specific point of the physical domain is related to the instantaneous turbulent kinetic energy, defined as

$$k = \frac{1}{2} u_i' u_i' \tag{6.1}$$

Multiplying the momentum equation by u_i' and summing over i, one can derive the transport equation for k

$$\frac{\partial \langle k \rangle}{\partial t} + \frac{\partial \langle k v' \rangle}{\partial y} + \frac{1}{\rho} \frac{\partial \langle p' v' \rangle}{\partial y} - \nu \frac{\partial^2 \langle k \rangle}{\partial y^2} = -\langle u' v' \rangle \frac{\partial U}{\partial y} - \nu \langle \frac{\partial u_i'}{\partial x_j} \frac{\partial u_i'}{\partial x_j} \rangle \tag{6.2}$$

Clearly, for a statistically stationary flow, the time derivative is equal to zero. The terms on the right-hand side of the previous equation are respectively the inertial, the pressure and viscous diffusion transports of turbulent kinetic energy. The terms on the left-hand side are the production and the rate of pseudo-dissipation. They represent respectively a source and a sink of turbulent kinetic energy.

The different terms in the turbulent kinetic energy transport equation are reported in Figure 6.1. In order to appreciate the characteristic flow features introduced by the wavy boundary a direct numerical simulation of a turbulent channel at $Re_\tau = 300$ is taken as reference (Cimarelli & De Angelis, 2011). Compared to wall turbulence, the magnitude of dissipation is generally reduced with a particular decrease in the water waves proximity. This lower dissipative nature of the flow is combined with a production peak slightly higher and shifted toward the boundary layer core. The total effect therefore is a turbulent kinetic energy excess between $13 < y^+ < 50$, which is carried away by the transport terms. The negative value of the transport indicates the extraction while the positive values indicates the supply

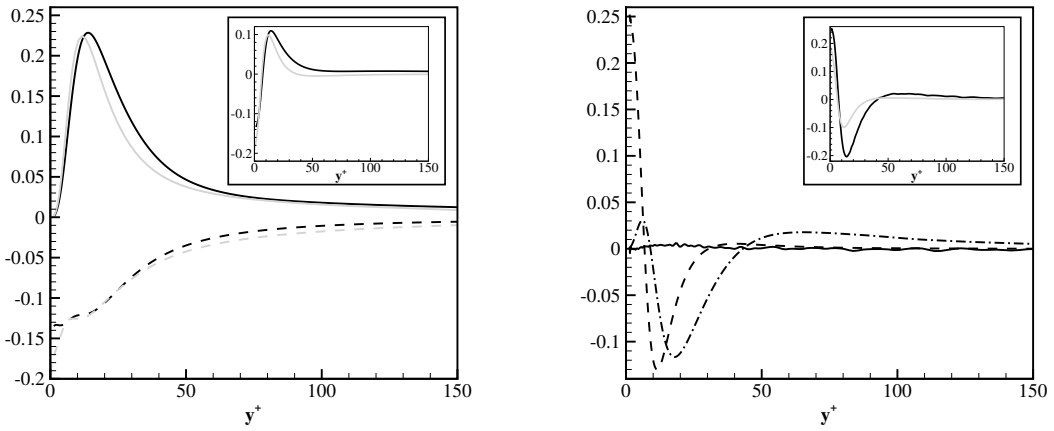

(a) (b)

Figure 6.1: (a) Turbulent kinetic energy budget vs. distance from the wall y^+: production (solid line), total transport (dashed line) and dissipation(dashed-dot line). (b) Different contributions to the turbulent kinetic energy transport vs. distance from the wall y^+: inertial transport (dashed-dot line), pressure transport (solid line) and viscous transport (dashed line).

of energy to the corresponding region. Figure 6.1 (b) displays the different contributions to the transport. In the proximity of the energy excess the total trasport term has a negative value and turbulent kinetic energy is drained thanks to the inertial and viscous components. Compared with wall-turbulence, an higher quantity of energy is supplied in the bulk region. The positive value of the transport term is mainly due to the inertial component which is the only effective contribution while the viscous and pressure components are nearly zero . Approaching the wall, where the production decreases and the dissipation grows, the transport term becomes positive and the energy supply is provided only by the viscous transport.

Introducing the total flux of turbulent kinetic energy:

$$\Phi = \langle kv' \rangle + \frac{1}{\rho}\langle p'v' \rangle - \nu \frac{\partial \langle k \rangle}{\partial y} \tag{6.3}$$

the turbulent kinetic equation can be rewritten as

$$\frac{\partial \Phi}{\partial y} = -\langle u'v' \rangle \frac{\partial U}{\partial y} - \nu \langle \frac{\partial u_i'}{\partial x_j} \frac{\partial u_i'}{\partial x_j} \rangle \tag{6.4}$$

Figure 6.2 shows the different contributions to the energy flux as a function of the distance from the wall. A negative value of the flux corresponds a flux transfers

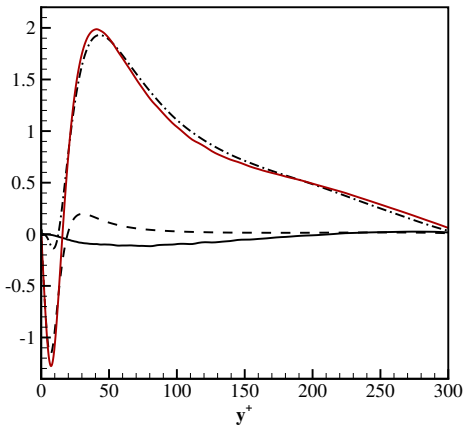

Figure 6.2: Different contributions to the flux of turbulent kinetic energy as a function of the distance from the wall y: inertial component (dashed-dotted), pressure transport (solid line), viscous transport (dashed-dotted line) and the total flux (red solid line).

energy toward the wall while a positive value to a flux transfers energy toward the bulk. Figure 6.2 show that only a part of the energy produced in the buffer region is sent toward the water free surface mainly by the viscous component and finally dissipated. As a matter of fact, due to the lower dissipative nature of the water surface, the energy excess tends rather to migrate toward the bulk thanks to the inertial component of the flux.

Chapter 7

The generalized Kolmogorov equation

In analogy with wall-turbulence, the presence of the water free surface under the wind turbulent boundary layer induces anisotropy and inhomogenity of the air flow. These flow features are respectively reflected in a turbulence production process taking place in the water proximity and in a spatial redistribution of turbulent kinetic energy in the whole domain. Nevertheless the complete dynamics of the turbulence processes can not be described in physical space alone. As a matter of fact, turbulence is characterized by flow structures and eddies whose size ranges from the characteristic width of the flow, L, to much smaller scales, which become progressively smaller as the Reynolds number increases. This multi-scale nature of turbulence is crucial to understand turbulent processes such as energy production, transport and dissipation which depend both on the position in the geometric space and on the turbulent scale considered. For this reason the turbulent kinetic energy equation is insufficient to describe completely the turbulent dynamics. The terms of the equation are indeed single-point observables: they depend only on the water free surface distance. In order to properly analyze turbulence, a quantity describing the flow dynamics both in physical and in scale space, has to be considered. As two-point statistical observable, we select the so called second order structure function defined as

$$\delta u^2 = \delta u_i \delta u_i \tag{7.1}$$

where $\delta u_i = u_i(x_s + r_s) - u_i(x_s)$ is the fluctuating velocity increment between points x_i' and x_i. These quantities represents a measure of the amount of kinetic energy at scale $r = \sqrt{r_i r_i}$ and depend both on separation vector r_i and on the spatial location of the mid-point $X_{ci} = 1/2(x_i' + x_i)$, as sketched in Figure 7.1. It is possible to derive from the Navier-Stokes equations a balance equation for the second structure function in globally anisotropic and inhomogeneous conditions.

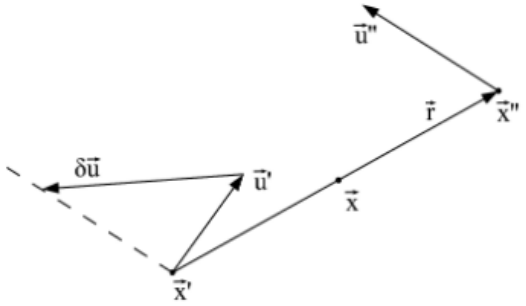

Figure 7.1: Sketch of the two-point velocity increment.

$$\frac{\partial\langle\delta u^2\rangle}{\partial t}+\frac{\partial\langle\delta u^2\delta u_j\rangle}{\partial r_j}+\frac{\partial\langle\delta u^2\delta U_j\rangle}{\partial r_j}+2\langle\delta u_i\delta u_j\rangle\frac{\partial\delta U}{\partial r_j}+\frac{\partial\langle u_j^*\delta u^2\rangle}{\partial X_{cj}}+\frac{\partial\langle\delta u^2U_j^*\rangle}{\partial X_{cj}}+$$
$$2\langle u_j^*\delta u_i\rangle\frac{\partial\delta U}{\partial X_{cj}}=-4\langle\epsilon^*\rangle+2\nu\frac{\partial\langle\delta u^2\rangle}{\partial r_i\partial r_i}-\frac{2}{\rho}\frac{\partial\langle\delta p\delta u_i\rangle}{\partial X_{ci}}+\frac{\nu}{2}\frac{\partial^2\langle\delta u^2\rangle}{\partial X_{cj}^2} \tag{7.2}$$

The previous equation, usually called generalized Kolmogorov equation, allows to identify all the processes which characterize the dynamics of inhomogeneous anisotropic flows both in the space of scales and in the physical space. In particular, the terms with r-derivatives describe physical processes which transfer energy through scales while those with x-derivatives arise due to inhomogeneities and describe physical processes which transfer energy through different regions of the flow. The generalized Kolmogorov equation specialized for the wind turbulent boundary layer over a wavy surface reduces to the formulation of the Kolmogorov equation in a turbulent channel once the water and air portion of the domain are consdered separately. Horizontal homogeneity yields $\partial\langle\cdot\rangle/\partial X_c=0$ and $\partial\langle\cdot\rangle/\partial Z_c=0$ while the stationary state condition leads to $\partial\langle\cdot\rangle/\partial t=0$

$$\frac{\langle\partial\delta u^2\delta u_i\rangle}{\partial r_i}+\frac{\langle\partial\delta u^2\delta U\rangle}{\partial r_x}+2\langle\partial u\partial v\rangle\left(\frac{dU}{dy}\right)^*+\frac{\partial\langle v^*\delta u^2\rangle}{\partial Y_c}=$$
$$-4\langle\epsilon^*\rangle+2\nu\frac{\partial^2\langle\partial u^2\rangle}{\partial r_i\partial r_i}-\frac{2}{\rho}\frac{\partial\langle\delta p\delta v\rangle}{\partial Y_c}+\frac{\nu}{2}\frac{\partial^2\langle\delta u^2\rangle}{\partial Y_c^2} \tag{7.3}$$

where $U(y)$ is the longitudinal mean velocity, $*$ denotes a mid-point average, $\langle\epsilon\rangle=\nu(\partial u_i/\partial x_j)(\partial u_i/\partial x_j)$ is the viscous pseudo-dissipation, $\langle\cdot\rangle$ denotes the average in the homogeneous directions and the Y_c is associated with inhomogeneity in the normal direction with respect to the water free surface. Compared to the turbulent kinetic energy budget where its terms depend only on the distance from the interface, the

Kolmogorov equation is written in a for dimensional space (r_x, r_y, r_z, Y_c), called the augmented space. The terms with r-derivatives describe the rate of energy flux in the three-dimensional space of scales. They are due to turbulent fluctuations, mean motion and viscous diffusion:

$$\frac{\partial\langle\delta u^2\delta u_i\rangle}{\partial r_i} \qquad \frac{\partial\langle\delta u^2\delta U\rangle}{\partial r_x} \qquad 2\nu\frac{\partial^2\langle\delta u^2\rangle}{\partial r_i\partial r_i}$$

The terms with Y_c-derivatives describe the rate of energy fluxes in the normal direction because of inhomogenity. They are due to turbulent fluctuations, pressure-velocity correlation and viscous diffusion:

$$\frac{\partial\langle v^*\delta u^2\delta u_i\rangle}{\partial Y_c} \qquad \frac{2}{\rho}\frac{\partial\langle\delta p\delta v\rangle}{\partial Y_c} \qquad \frac{\nu}{2}\frac{\partial^2\langle\delta u^2\rangle}{\partial Y_c^2}$$

This double energy flux balance with the behaviour in the augmented space of the energy source due to the anisotropic production by mean shear

$$2\langle\delta u\delta v\rangle\left(\frac{dU}{dy}\right)^*$$

and of the energy sink due to viscous dissipation,

$$4\langle\epsilon^*\rangle \quad .$$

7.1 The flow of energy in the augmented space

The generalized Kolmogorov equation introduced in the previous section is a tool to describe the turbulence phenomena taking place in the space of scale and in the physical space. This equation can be recast in a conservative form as:

$$\nabla\cdot\mathbf{\Phi}(r, Y_c) = \xi(r, Y_c) \tag{7.4}$$

where $\nabla\cdot\mathbf{\Phi}$ is the four-dimensional divergence, ξ is the scale energy source/sink and $\mathbf{\Phi}$ is a four-dimesional vector representing the energy fluxes, called hyper-flux,

$$\mathbf{\Phi} = (\Phi_{rx}, \Phi_{ry}, \Phi_{rz}, \Phi_c).$$

The hyper-flux in the three-dimensional space of scale describes the energy flux among scales and it is called the three-dimensional energy transfer vector,

$$\mathbf{\Phi_r} = (\Phi_{rx}, \Phi_{ry}, \Phi_{rz}) = \langle\delta u^2\delta\boldsymbol{u}\rangle - 2\nu\nabla_r\langle\delta u^2\rangle.$$

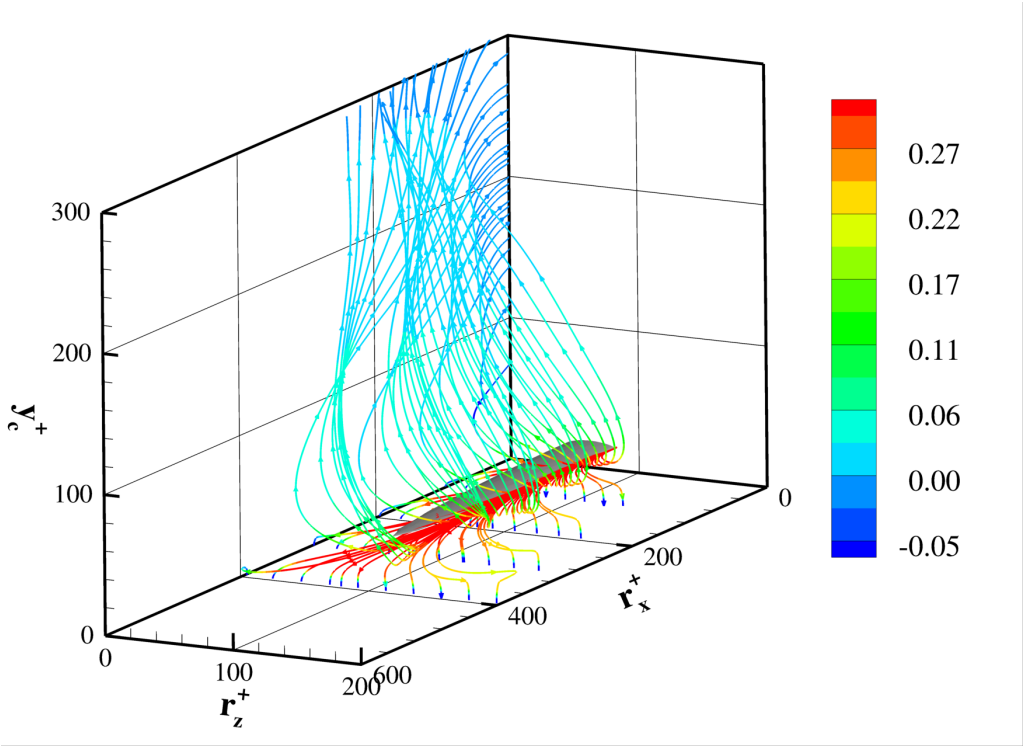

Figure 7.2: (r_x, r_z, Y_c)-projection $(r_y = 0)$ of the augmented phase-space. Streamlines of the inertial component of the reduced hyper-flux colored with the pseudo-source ξ_p. The gray iso-surface shows $\xi = 0.9\xi_{max}$ thus highlighting the source region of fluxes of the augmented space (r_x, r_z, Y_c).

The projection of the hyper-flux in the physical space is a pseudo-scalar and represents the spatial energy flux

$$\Phi_c = \langle v^* \delta u^2 \rangle + 2\langle \delta p \delta v \rangle - \nu/2 \partial \langle \partial u^2 \rangle / \partial Y_c.$$

The conservative form allows to appreciate in which region of the $(\boldsymbol{r}, Y_c)$ space the production term exceeds the dissipation rate $(\xi(\boldsymbol{r}, Yc) > 0)$ and where the consequential energy excess is brought to dissipate by means of the two scale-energy fluxes, namely $\boldsymbol{\Phi_r}$ through the scales of motion and Φ_c in physical space.

In figure 7.2 the scale-energy hyper-fluxes and the source ξ are shown in the augmented space (r_x, r_z, Y_c) for $r_y = 0$. In this subspace, the net scale energy drain and release by fluxes is given by a pseudo source term,

$$\xi_p = -2\langle \delta u \delta v \rangle \left(\frac{dU}{dy} \right)^* - 4\langle \epsilon^* \rangle - \frac{\partial \langle \delta u^2 \delta v \rangle}{\partial r_y} + 2\nu \frac{\partial^2 \langle \partial u^2 \rangle}{\partial r_y^2}$$

that is reported in figure 7.2 by coloring the field of fluxes. As for a wall-bounded flow, it is evident how the classical theory of turbulence fails near the water surface.

The turbulent energy is not introduced at large scales, but, the source term ξ reaches its maximum in a range of small scales well within the buffer region (gray isosurface). From that region the scale-energy hyper-fluxes diverge to feed larger scales before bending towards the water surface and towards the bulk of the wind boundary layer. The paths of fluxes moving towards the water surface become aligned to the vertical direction thus showing that the dissipative sink represented by the water surface is distributed at a variety of interface-parallel scales being a forward cascade towards small scales absent. On the other hand, the paths of fluxes moving towards the core of the wind boundary layer follow a spiral path thus sustaining longer and wider turbulent structures while ascending before eventually bending towards small scales where dissipation occurs. Such a scenario conforms with that observed in wall turbulence (Cimarelli *et al.*, 2013).

Chapter 8

Conclusions

A Direct Numerical Simulation of the wind-wave interaction problem has been performed. To the author' knowledge, the simulation represents one of the very first attempts to get the fully-coupled solution of the wind-wave problem based on first principles and on realistic values of the fluid properties of air and water. The considered flow settings consist of a two-phase open channel flow driven by a constant pressure gradient where the wind is turbulent and the water is almost quiescent. The simplicity of the flow settings is such that the complex problem of wind turbulence over water waves essentially reduces to be governed by a single parameter, the wind friction Reynolds number $Re_{\tau_a} = 317$.

The simulation reveals an interesting water wave pattern. It consists of waves at very low steepness and elevation ($S = 7.3 \cdot 10^{-4}$ and $\delta_w^+ = 0.3$) propagating at an angle $\gamma = 38.6°$ in the upwind direction with a phase speed $\boldsymbol{c}^+ \approx (-10, -8)$. Despite the small size of the water wave pattern, its effect on the turbulent wind is far from being negligible. A significant reduction of drag is indeed observed, $\Delta B = 1.6$. The origin of drag reduction is associated with the presence of a wave-induced Stokes sublayer. The oblique wave pattern is found to induce periodically distributed pressure gradients also in the spanwise direction thus leading to an oscillating spanwise forcing. Such type of modulation gives rise to a weakening of the self-sustaining processes of turbulence in the very near-interface region and, hence, to drag reduction. It is remarkable the significant effect on the turbulent wind despite the very small thickness of the Stokes layer $\ell_s^+ \approx 2$ and the very weak intensity of the associated motion $|w|_{max}^+ \approx 10^{-3}$.

Both the mean velocity and turbulent profiles agree with the presence of a near-interface weakening of turbulence due to the wave-induced Stokes sublayer. An upward shift of the self-sustaining processes is indeed observed. A consequence of this shift is the observed increase in size of the main turbulent structures composing the autonomous cycle of turbulence, i.e. quasi-streamwise vortices 53 viscous units wide and streamwise velocity streaks 2800 viscous units long. The study of

the field of stresses reveals that despite the very small thickness of the Stokes sub-layer, its effect on the pressure field is felt in the wind boundary layer also at very large distances from the interface. Indeed, the two-point correlation function clearly highlights the non-local nature of wind-wave induced pressure fluctuations that are shown to penetrate the wind boundary layer up to $y^+ \approx 60$. On the contrary, the field of shear stresses induced by wind-wave interactions phenomena remains more confined to the water surface region. These effects emerge in a change of sign of the Reynolds shear stresses $-\langle u'v' \rangle < 0$ for $y^+ < 1$ that is clearly induced by the non-sheltering behaviour of the wind over the very low steepness and elevation of the developed water waves. Also the two-point correlation function confirms this scenario highlighting that wind-wave interaction effect on the shear stresses remains confined to the very near-interface region for $y^+ < 3$.

To close this work, it is important to note that the simulated flow conditions are far from the intense events occurring at the ocean-atmosphere interface. However, the simplicity of the flow settings allows us to reduce the complex problem of wind-wave interactions to its essential features thus unveiling very basic flow phenomena that may explain some experimental evidences also in real wind-wave problems. An example is the finding of the wave-induced Stokes layer. Such phenomenon is here unveiled to be at the basis of a change of the momentum flux at the air-water interface. It is then possible to argue that a similar phenomenon can be responsible also for the large scatter of the drag coefficient data in field measurements. Indeed, the condition for the development of the Stokes sub-layer is a misalignment of the wind with respect to water waves. In this context, it is well-known that field realizations are characterized by the presence of swell waves from remote wind-generation events. Swell waves move in arbitrary directions with respect to the local wind and their interaction with local wind waves often lead to a water surface pattern misaligned with the wind direction. Hence, it is reasonable to assume that a Stokes sublayer often develops in field realizations thus modifying the air-sea momentum flux with respect to that of water waves aligned with the wind that is known to be generally increased with respect to flat surfaces. These arguments suggest to analyse field measurements of the drag coefficient as a function of the angle between wind and waves.

Bibliography

Abe, H., Kawamura, H. & Matsuo, Y. 2001 Direct numerical simulation of a fully developed turbulent channel flow with respect to the Reynolds number dependence. *J. Fluids Eng.* **123** (2), 382–393.

Belcher, S. E. & Hunt, J. C. R. 1993 Turbulent shear flow over slowly moving waves. *J. Fluid Mech.* **251**, 109–148.

Brackbill, J. U., Kothe, D. B. & Zemach, C. 1992 A continuum method for modeling surface tension. *J. Comput. Phys.* **100** (2), 335–354.

Cao, T. & Shen, L. 2021 A numerical and theoretical study of wind over fast-propagating water waves. *J. Fluid Mech.* **919**.

Caulliez, G. & Collard, F. 1999 Three-dimensional evolution of wind waves from gravity-capillary to short gravity range. *Eur. J. Mech. B-Fluid* **18** (3), 389–402.

Cimarelli, A. & De Angelis, E. 2011 Analysis of the kolmogorov equation for filtered wall-turbulent flows. *J. Fluid Mech.* **676**, 376–395.

Cimarelli, A., De Angelis, E. & Casciola, C.M. 2013 Paths of energy in turbulent channel flows. *J. Fluid Mech.* **715**, 436–451.

Druzhinin, O. A., Troitskaya, Y. I. & Zilitinkevich, S. S. 2012 Direct numerical simulation of a turbulent wind over a wavy water surface. *Journal of Geophysical Research: Oceans* **117** (C11).

Ghebali, S., Chernyshenko, S. I. & Leschziner, M. A. 2017 Can large-scale oblique undulations on a solid wall reduce the turbulent drag? *Phys. Fluids* **29** (10), 105102.

Hara, T. & Karachintsev, A. V. 2003 Observation of nonlinear effects in ocean surface wave frequency spectra. *J. Phys. Oceanogr.* **33** (2), 422–430.

Hirt, C. W. & Nichols, B. D. 1981 Volume of fluid (VOF) method for the dynamics of free boundaries. *J. Comput. Phys.* **39** (1), 201–225.

Hwang, P. A. & Wang, D. W. 2001 Directional distributions and mean square slopes in the equilibrium and saturation ranges of the wave spectrum. *J. Phys. Oceanogr.* **31** (5), 1346–1360.

Hwang, P. A., Wang, D. W., Yungel, J., Swift, R. N. & Krabill, W. B. 2019 Do wind-generated waves under steady forcing propagate primarily in the downwind direction? *arXiv preprint arXiv:1907.01532* .

Issa, R. I. 1986 Solution of the implicitly discretised fluid flow equations by operator-splitting. *J. Comput. Phys.* **62** (1), 40–65.

Jeffreys, H. 1925 On the formation of water waves by wind. *Proceedings of the royal society of London. Series A, containing papers of a mathematical and physical character* **107** (742), 189–206.

Jeong, J., Hussain, F., Schoppa, W. & Kim, J. 1997 Coherent structures near the wall in a turbulent channel flow. *J. Fluid Mech.* **332**, 185–214.

Jimenez, J. & Pinelli, A. 1999 The autonomous cycle of near-wall turbulence. *J. Fluid Mech.* **389**, 335–359.

Kihara, N., Hanazaki, H., Mizuya, T. & Ueda, H. 2007 Relationship between airflow at the critical height and momentum transfer to the traveling waves. *Phys. Fluids* **19** (1), 015102.

Kim, J., Moin, P. & Moser, R. 1987 Turbulence statistics in fully developed channel flow at low reynolds number. *J. Fluid Mech.* **177**, 133–166.

Liu, H.-R., Chong, K. L., Yang, R., Verzicco, R. & Lohse, D. 2022 Heat transfer in turbulent Rayleigh–Bénard convection through two immiscible fluid layers. *J. Fluid Mech.* **938**.

Miles, J. W. 1957 On the generation of surface waves by shear flows. *J. Fluid Mech.* **3** (2), 185–204.

Morland, L. C. 1996 Oblique wind waves generated by the instability of wind blowing over water. *J. Fluid Mech.* **316**, 163–172.

Nagaosa, R. & Handler, R. A. 2003 Statistical analysis of coherent vortices near a free surface in a fully developed turbulence. *Phys. Fluids* **15** (2), 375–394.

Okagaki, Y., Yonomoto, T., Ishigaki, M. & Hirose, Y. 2021 Numerical study on an interface compression method for the volume of fluid approach. *Fluids* **6** (2), 80.

Phillips, O. M. 1957 On the generation of waves by turbulent wind. *J. Fluid Mech.* **2** (5), 417–445.

Plant, W. J. & Wright, J. W. 1980 Phase speeds of upwind and downwind traveling short gravity waves. *J. Geophys. Res.: Oceans* **85** (C6), 3304–3310.

Pope, S. B. 2000 *Turbulent flows*. Cambridge university press.

Quadrio, M. & Ricco, P. 2011 The laminar generalized Stokes layer and turbulent drag reduction. *J. Fluid Mech.* **667**, 135–157.

Quadrio, M., Ricco, P. & Viotti, C. 2009 Streamwise-travelling waves of spanwise wall velocity for turbulent drag reduction. *J. Fluid Mech.* **627**, 161–178.

Scapin, N., Demou, A. D. & Brandt, L. 2022 Evaporating Rayleigh-B\'enard convection: prediction of interface temperature and global heat transfer modulation. *arXiv preprint arXiv:2205.02710* .

Shemer, L. 2019 On evolution of young wind waves in time and space. *Atmosphere* **10** (9), 562.

Sullivan, P. P., McWilliams, J. C. & Moeng, C. 2000 Simulation of turbulent flow over idealized water waves. *J. Fluid Mech.* **404**, 47–85.

Sullivan, P. P., McWilliams, J. C. & Patton, E. G. 2014 Large-eddy simulation of marine atmospheric boundary layers above a spectrum of moving waves. *Journal of the Atmospheric Sciences* **71** (11), 4001–4027.

Touber, E. & Leschziner, M. A. 2012 Near-wall streak modification by spanwise oscillatory wall motion and drag-reduction mechanisms. *J. Fluid Mech.* **693**, 150–200.

Walsh, E. J., Hancock, D. W., Hines, D. E., Swift, R. N. & Scott, J. F. 1985 Directional wave spectra measured with the surface contour radar. *J. Phys. Oceanogr.* **15** (5), 566–592.

Walsh, E. J., Hancock, D. W., Hines, D. E., Swift, R. N. & Scott, J. F. 1989 An observation of the directional wave spectrum evolution from shoreline to fully developed. *J. Phys. Oceanogr.* **19** (5), 670–690.

Wang, D. W. & Hwang, P. A. 2004 The dispersion relation of short wind waves from space–time wave measurements. *J. Atmos. Ocean. Tech.* **21** (12), 1936–1945.

Yang, D., Meneveau, C. & Shen, L. 2013 Dynamic modelling of sea-surface roughness for large-eddy simulation of wind over ocean wavefield. *J. Fluid Mech.* **726**, 62–99.

Yang, D. & Shen, L. 2009 Characteristics of coherent vortical structures in turbulent flows over progressive surface waves. *Phys. Fluids* **21** (12), 125106.

Yang, D. & Shen, L. 2011 Simulation of viscous flows with undulatory boundaries: Part II. Coupling with other solvers for two-fluid computations. *J. Comp. Phys.* **230** (14), 5510–5531.

Yang, D. I. & Shen, L. 2010 Direct-simulation-based study of turbulent flow over various waving boundaries. *J. Fluid Mech.* **650**, 131–180.